UNIVERSIDADE
BEIRA INTERIOR

Effects of Wing-Fuselage Interface Position on Lift and Drag
(versão final após defesa)

Rodrigo Manuel Cação do Carmo Bombas

Dissertação para Obtenção do Grau de Mestre em
Engenharia Aeronáutica
(2º ciclo de estudo)

Orientador: Prof. Doutor Pedro Vieira Gamboa

Dezembro 2025

Declaração de Integridade

Eu, Rodrigo Manuel Cação do Carmo Bombas, que abaixo assino, estudante com o número de inscrição 45824 de/o Engenharia Aeronáutica da Faculdade de Engenharia, declaro ter desenvolvido o presente trabalho e elaborado o presente texto em total consonância com o **Código de Integridades da Universidade da Beira Interior**.

Mais concretamente, afirmo não ter incorrido em qualquer das variedades de Fraude Académica, e que aqui declaro conhecer, que em particular atendi à exigida referenciação de frases, extratos, imagens e outras formas de trabalho intelectual, e assumindo assim na íntegra as responsabilidades da autoria.

Universidade da Beira Interior, Covilhã 30/12/2025

Assinado por: **Rodrigo Manuel Cação do Carmo Bombas**
Num. de Identificação: 15597693
Data: 2025.12.30 21:48:30+00'00'

(assinatura conforme Cartão de Cidadão ou preferencialmente assinatura digital no documento original se naquele mesmo formato)

Acknowledgements

I express the most profound gratitude towards my Supervisor Professor Doctor Pedro Gamboa, for the opportunity of working with him on developing this topic, and for his availability and ever insightful advice. I am also thankful for the resources and technical assistance brought to my disposal, without which this dissertation would not be possible.

The most sincere thanks to my father and to my aunt, for listening to my unending discussions with myself, and for giving me the assurances and confidence needed for the extra effort I put into this work.

Thank you to my friends for organising the impromptu ”strategic framing meetings” without which I would not have had as much fun as I did during the process.

Resumo

O efeito de interferência entre dois componentes de uma aeronave tem vindo, com o aumento da eficiência aerodinâmica evidenciado nas últimas décadas, a ser cada vez mais relevante no processo de projeto. De forma a compreender como este se manifesta em aeronaves de pequenas dimensões e em baixo número de Reynolds, foi realizado um estudo da posição da asa na fuselagem, assim como da influência de carenagens de interface entre os dois componentes e da secção da fuselagem no arrasto de interferência.

Procurando determinar quais a posições da interface entre a asa e a fuselagem mais favoráveis ao arrasto e à sustentação, incluindo ainda dois tipos de carenagem e de secção da fuselagem, a aeronave disponibilizada pela equipa UBIAT foi modelada em *CATIAV5*, obtendo um modelo simplificado mas que retém as características da aeronave real. Foi depois preparado em *Ansys Discovery* para estabelecer o corpo de influência, o volume de simulação e as condições-fronteira. Este *setup* é então importado para *Ansys Fluent*, onde a malha é gerada de acordo o estudo de independência de malha realizado. A simulação CFD é feita utilizando o modelo $k - \omega$ SST com parâmetros standard e correções para regime de transição e baixos valores de número de Reynolds.

Foram analisadas quatro configurações da interface asa-fuselagem além da original: duas verticais e duas horizontais. As posições verticias foram ainda analizadas com carenagens e com uma secção da fuselagem circular. Os resultados relativos à posição da interface para ambas as secções de fuselagem consideram-se dentro das expectativas e apoiados pela bibliografia. No que respeita à introdução de carenagens, verificou-se que ambas influenciam positivamente a eficiência aerodinâmica, apesar dos resultados não refletirem a bibliografia.

As conclusões principais a retirar deste trabalho são a vantagem da asa alta numa interface com fuselagem quadrada e da asa média numa interface com fuselagem circular. A initrodução de carenagens resultou num aumento de até 4.7% na eficiência aerodinâmica para uma configuração em asa alta e de secção de fuselagem quadrangular, sendo desprezível para as restantes posições verticais.

Palavras-chave

Arrasto de Interferência, CFD, Carenagens, Secção da Fuselagem

Abstract

The interference effect between two aircraft components has become increasingly relevant in the design process, in parallel with the advances in aerodynamic efficiency observed over the last decades. In order to understand how this phenomenon manifests itself in small aircraft operating at low Reynolds numbers, a study was carried out on the influence of wing position relative to the fuselage, as well as the effect of fairings at the interface between the two components and the fuselage cross-section on interference drag.

To determine the most favourable wing–fuselage interface positions in terms of drag and lift—considering also two types of fairings and fuselage cross-sections—the aircraft provided by the UBIAT team was modelled in *CATIAV5*. A simplified model was developed that nonetheless preserved the essential features of the real aircraft. The geometry was then prepared in *Ansys Discovery* to define the body of influence, the simulation volume, and the boundary conditions. This setup was subsequently imported into *Ansys Fluent*, where the computational mesh was generated according to a previously conducted mesh-independence study. The CFD simulations were performed using the k–ω SST turbulence model with standard parameters, including corrections for transitional flow and low Reynolds number regimes.

Four alternative wing–fuselage interface configurations, in addition to the baseline case, were analysed: two vertical and two horizontal. The vertical configurations were further assessed with fairings and with a circular fuselage cross-section. The results regarding wing–fuselage positioning for both fuselage geometries were consistent with expectations and supported by literature. As for the introduction of fairings, both were found to improve aerodynamic efficiency, although the results did not fully align with published references.

The main conclusions drawn from this work are the advantage of a high-wing configuration when interfaced with a square fuselage cross-section, and of a mid-wing configuration when interfaced with a circular fuselage cross-section. The addition of fairings yielded improvements of up to 4.7% in aerodynamic efficiency for the high-wing configuration with a square-section fuselage, while their effect was negligible for the other vertical positions.

Keywords

Interference Drag, CFD, Fairings, Fuselage Cross-Section

Contents

List of Figures

List of Tables

Glossary

A	Axial Force	P_i	Local Stagnation Pressure
α	Angle of Attack	P_{i_∞}	Free Stream Stagnation Pressure
c	Wing Chord	P_∞	Free Stream Static Pressure
C_D	Drag Coefficient	r	Shear Forces
C_L	Lift Coefficient	R	Aerodynamic Force
$C_{L_{max}}$	Maximum Lift Coefficient	ρ	Density
D	Drag	s	Surface Distance
D_1	Drag of Component 1	s_{ref}	Wing Planform Area
D_2	Drag of Component 2	σ	Velocity Gradient
$D_{1\|2}$	Configuration Total Drag	τ_l	Lower Surface Shear Force
ΔD	Interference Drag	τ_u	Upper Surface Shear Force
d_{s_l}	Increment of Area of Lower Surface	T_i	Local Stagnation Temperature
		T_{i_∞}	Free Stream Stagnation Temperature
d_{s_u}	Increment of Area of Upper Surface	U^*	Artificial Velocity
L	Lift	U_∞	Free Stream Velocity Vector
L_f	Fuselage Length	u_b	Blockage Velocity
M	Moment	V	Local Velocity Vector
M_∞	Free Stream Mach Number	V_∞	Free Stream Velocity
N	Normal Force	θ	Angle Relative to Vertical Axis
p	Pressure Forces	ζ	Trailing Vorticity
P	Local Static Pressure	γ	Specific Heat Ratio

Acronyms

ACC	Air Cargo Challenge
AOA	Angle of Attack
CAD	Computer Assisted Design
CFD	Computational Fluid Dynamics
LSB	Laminar Separation Bubble
MALE	Medium-Altitude Long-Endurance
NACA	National Advisory Committee for Aeronautics
NSE	Navier–Stokes Equations
OHS	Outboard Horizontal Stabilizer
UAV	Unmanned Aerial Vehicle
UBI	Universidade da Beira Interior

Chapter 1

Introduction

1.1 Motivation

During the last decade, Unmanned Aerial Vehicles (UAVs) have become highly adaptable and diverse instruments in most human activities , such as military, agricultural, research and others. Current trends indicate that technological advancements have allowed for the reduction of weight, size, and complexity of UAVs, increasing their accessibility and flexibility [1]. While these characteristics are of great importance for the consumer, they present engineering challenges that must be overcome.

The great reduction in size that UAVs have undergone for the better part of half a century often means that the UAVs fly in a relatively low Reynolds number interval, 2×10^5 to 5×10^5, which coincides with the transition regime from laminar to turbulent flow. While this process is hard to predict and can result in both great increases in drag and abrupt stall characteristics, especially in the wing-fuselage interface [2], it can be reduced through the vertical positioning of the wing and the use of wing-fuselage fairings [3].

The scope of this thesis lies, then, in the study of wing-fuselage interference effect, and how it may contribute to the total drag of a UAV, given the wing position and wing-fuselage fairings. While work such as this has been previously conducted by the National Advisory Committee for Aeronautics (NACA) in the earlier half of the 20th century, it was conducted in a wind tunnel with large-scale mockups, when UAVs were not yet widely employed. As such, most data available does not contemplate the Reynolds number interval where most commercially available UAVs operate.

1.2 Objectives

The main objective of this dissertation is to numerically calculate the lift and drag coefficient in an aircraft flying at low-Reynolds conditions for several different configurations of the wing-fuselage interface and positions. Specifically, it aims to compare the several analysed instances and ascertain which combination of wing position and fairing produces the least interference drag for specified operating conditions.

To achieve this objective, several specific goals have been defined:

- Establish the baseline knowledge gathered in this scope, either by organisations or individuals;
- Define the most commonly used platform for commercially available UAVs, from which to compare the achieved results;
- Develop and document the methodologies through which to analyze the different configurations of the aircraft wing-fuselage interface;
- Validate the obtained results by comparison with eligible work;
- Allow for the systematisation of the obtained results, and therefore the qualitative comparison of the analysed configurations.

1.3 Thesis Outline

After this first introductory chapter, in which the motivation and objectives of this dissertation are presented and described, a brief description of the following chapters is presented:

- **Chapter 2** presents the bibliographic review on the existing literature on aerodynamic drag, focusing on the interference effects created by the wing-fuselage interface. Fundamental aerodynamic principles are discussed, as well as experimental and numerical studies used for drag analysis. One of the sections is dedicated to low-Reynolds flow characteristics, such as laminar and turbulent separations, in addition to the phenomenon of transition. This review identifies certain trends in the current research which this work aims to expand upon. It also entails the computational methodology generally employed for the study of interference drag. It aims to describe the governing equations, turbulence models and numerical approaches used in CFD (Computational Fluid Dynamics) simulations.
- **Chapter 3** explores computational tools, meshing strategies and boundary conditions, aiming to approximate the results to reality as much as possible. It also outlines the various tested configurations, alongside grid independence studies and validation efforts, which are essential for the following validation of these results.
- **Chapter 4** presents the results of the CFD simulations, analysing aerodynamic interactions in the models, pressure distributions, drag breakdowns and lift/drag distributions. The differences between several configuration parameters are analysed and validation is achieved by comparison with experimental data from previous research. A general qualitative system for comparing the various configurations is developed.

- **Chapter 5** concludes this dissertation with a summary of findings, allowing the analysis of their implications in aircraft design. Key takeaways are made for minimising interference drag based on the acquired results. This chapter also discusses the limitations of this work and suggests future research.

Chapter 2

Bibliographic Review

In this chapter, the underlined fundamental theoretical concepts set the basis upon which to build the methodology used in this dissertation, as well as provide the context needed for the computational simulations presented in *Chapter 3*.

Chapter 2.1 presents a breakdown of the commonly categorised types of drag, with a specificity for interference drag. *Chapter 2.2* explores the various approaches, both numerical and experimental, for drag and drag coefficient calculations, lightly overviewing their advantages and limitations. *Chapter 2.3* dives into the existing work on wing-fuselage interference drag, presenting relevant experimental and numerical results. Lastly, *Chapter 2.4* presents commonly used concepts and methodologies that will prove useful in simulating the required airflows with acceptable degree of precision.

2.1 Fundamentals of Aerodynamic Drag

For any given body in relative motion within a fluid (take an aerofoil as an example), aerodynamic forces and moments are transmitted entirely to said body through pressure and shear stress distributions over its surface (*Figure 2.1a*). When integrated over the entire surface area, they yield a net force and moment on the body (*Figure 2.1b*), of which the force can be divided into two sets of two forces [4].

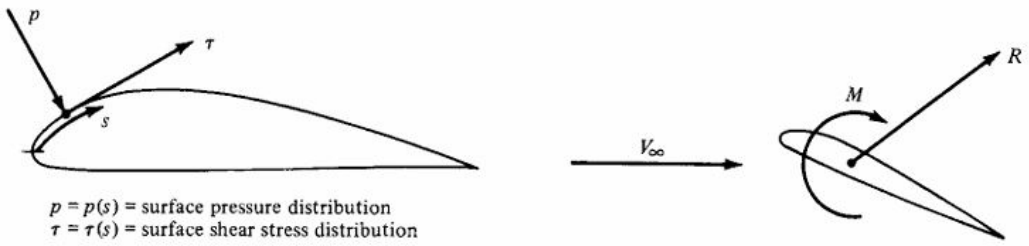

(a) Illustration of pressure and shear stress on an aerodynamic surface.

(b) Resultant aerodynamic force and moment on the body.

Figure 2.1: Representation of aerodynamic force generation on a body immersed in uniform flow. Adapted from Anderson.

Taking into account the freestream velocity of the body, V_∞, and its chord, there are two ways to represent the aerodynamic force, R, by its components: by taking the direction of V_∞ as the horizontal reference axis or by taking the chord direction as the horizontal reference axis (*Figure 2.2*). For the purposes of this dissertation, the reference system is

considered to be based on the freestream velocity vector, $\vec{V}_\infty$.

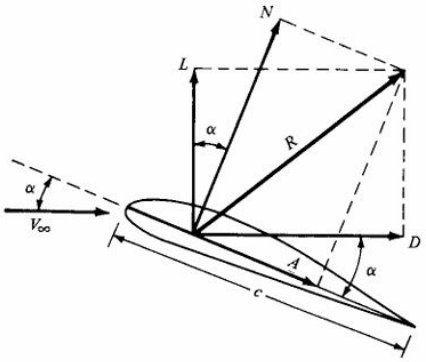

Figure 2.2: Resultant aerodynamic force and the components into which it splits. Adapted from Anderson.

Anderson [4] defines the aerodynamic lift and drag components as functions of the normal force N, the axial force A, with respect to the geometric chord, and the angle of attack α (*Equation 2.1*).

$$\begin{aligned} L &= N\cos\alpha - A\sin\alpha \\ D &= N\sin\alpha + A\cos\alpha \end{aligned} \tag{2.1}$$

When integrating both the normal and axial forces with respect to the geometric chord over the body surface, N' and A', which represent force per unit span, can be determined with *Equation 2.2*.

$$\begin{aligned} N' &= -\int_{\text{LE}}^{\text{TE}} (p_u\cos\theta + \tau_u\sin\theta)\,ds_u + \int_{\text{LE}}^{\text{TE}} (p_l\cos\theta - \tau_l\sin\theta)\,ds_l \\ A' &= \int_{\text{LE}}^{\text{TE}} (-p_u\sin\theta + \tau_u\cos\theta)\,ds_u + \int_{\text{LE}}^{\text{TE}} (p_l\sin\theta + \tau_l\cos\theta)\,ds_l \end{aligned} \tag{2.2}$$

where θ is the angle relative to the vertical axis, for pressure, and the horizontal axis, for shear stress, being positive clockwise and ds_u,ds_l are the increments of area, respectively, of the upper and lower surfaces, with respect to $\vec{V}_\infty$.

Thus, it is clear that the aerodynamic drag force can be mathematically defined as the sum of both pressure (or normal) and shear (or tangential) forces over a body's surface in the free stream direction. However, both these components can be manifested very differently in different bodies. Bodies that produce little to no lift will display a drag force composed of two main forms of drag: skin friction drag and form drag. Should the flow be mostly attached to the surface of said body, the main contribution to drag would be skin friction drag [3]. If the flow was, instead, mostly detached, the loss in momentum would be far

greater due to greater form drag. The sum of skin friction drag and form drag is called the profile drag. When bodies produce lift, there is a directly related drag component, called induced drag, that is generated. Induced drag is a result of the modification in the body pressure distribution with origins in the trailing vortex system that always accompanies the three-dimensional production of lift. At transonic and supersonic velocities, yet another drag-generating mechanism arises in the form of wave drag [5]. In the scope of this dissertation, since the velocity considered is quite low, wave drag does not manifest and is therefore negligible.

Raymer [3] defines a terminology matrix which provides the multiple definitions given to drag components, which are often confusing and used interchangeably. *Table 2.1* summarizes the relevant concepts presented above.

Table 2.1: Drag terminology matrix. Adapted from Raymer.

<table>
<tr><th></th><th rowspan="2">Shear Forces</th><th colspan="2">Pressure forces</th></tr>
<tr><th>Separation</th><th>Circulation</th></tr>
<tr><td rowspan="4">Parasite Drag</td><td>Skin friction</td><td rowspan="2">Viscous separation</td><td rowspan="3"></td></tr>
<tr><td>Scrubbing drag</td></tr>
<tr><td colspan="2">Interference drag</td></tr>
<tr><td rowspan="2"></td><td colspan="2">Profile drag</td></tr>
<tr><td rowspan="3">Drag due to Lift</td><td rowspan="3">Supervelocity effect on skin friction</td><td>Camber drag</td><td rowspan="2">Induced drag</td></tr>
<tr><td>Supervelocity effect on profile drag (e.g., landing gear)</td></tr>
<tr><td></td><td>Trim drag</td></tr>
</table>

Interference drag is defined as the drag force resultant of the mixing of two different boundary layers over different bodies. Usually, interference drag is greater than the sum of both bodies' individual drag forces, each measured in free flow. Mathematically, interference drag can be defined as $\Delta D = D_{1|2} - (D_1 + D_2)$. There are several phenomena associated with this drag-generating mechanism. One of the most common is the shielding effect, where two bodies immersed in a flow, one behind the other, present two different measurements for the drag force. This is explained by the reduced dynamic pressure within the wake of the first body interfering with the flow of the second body, resulting in a lower drag force [6]. Although this phenomenon is relevant in aircraft flying with a slip angle, where interference drag counts would be different for both wing-fuselage interfaces, the focus is specifically on the interference between the wing and the fuselage interface in no-slip flying conditions, meaning it is not very relevant for this work. However, in *Fluid - Dynamic Drag*, Hoerner [6] delves into the three-dimensional effects of interference drag between two components, establishing, based on experimental data, a series of empirical equations capable of estimating the order of magnitude of several different configurations of connections in an aircraft.

The author presents explanations for several phenomena related to wing-fuselage interfaces, specifically exploring situations where the longitudinal and vertical wing positions influence interference drag, and how this loss of energy in the interface can be mitigated up to 90% through the use of fairings. It is also concluded that a mid-wing configuration for a circular-section fuselage produces the least interference drag, should the dihedral

angle be zero [3].

Unlike Raymer, Hoerner indicates that the source of interference drag is both parasitic and induced, and that depending on the position of the wing, one can be more significant than the other. The notion of α *flow* is introduced, from whence it is stated that circulation from the wing root is transferred to the fuselage, resulting in increased lift at the root and, therefore, increased induced drag at the interface.

2.1.1 Low Reynolds Number Aerodynamics

It is well established that the aerodynamic behaviour of streamlined bodies varies significantly with the Reynolds number. Typically, high-Reynolds number aerofoils have degraded performance in low-Reynolds number conditions, often being outperformed by a flat plate [7].

Winslow *et al.* [7] have studied the effects of low-Reynolds number on conventional aerofoils and compared those results to flat plates of various thicknesses and cambers, which typically outperform conventional aerofoils in such conditions. Under these conditions, viscous forces have higher importance than the inertial forces, meaning boundary-layer related phenomena vary on the aerofoil. This indicates that simply scaling down conventional aerofoils yields poor results in terms of aerodynamic efficiency and increased drag. Flows in the 10^4 to 10^5 Reynolds number interval are dominated by laminar flow, which is subject to a significant adverse pressure gradient in the leading edge, leading to a separation of the laminar boundary-layer as a shear layer. This shear layer gains momentum from the freestream and reattaches to the aerofoil as a turbulent boundary-layer, creating a Laminar Separation Bubble (LSB). As the Reynolds number decreases from 10^5 to 5×10^4, the viscous forces become prominent, leading to an increase in size of both the LSB and the boundary-layer thickness, and, therefore, and increase in the aerofoil parasitic drag (*Figure 2.3*).

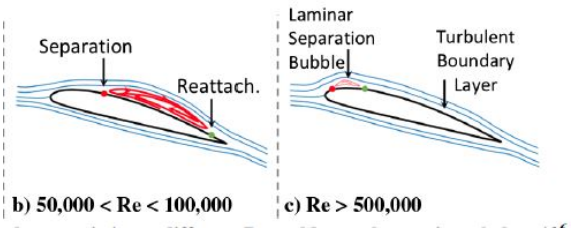

Figure 2.3: Illustration highlighting conventional airfoil separation characteristics at different Reynolds number regimes below 10^6. Adapted from Winslow.

Winslow *et al.* [7] state that previous experiments have proven that $C_{L_{max}}$ increases and the minimum drag coefficient decreases with a higher Reynolds number. It is also stated that the drag polar of aerofoils is virtually insensitive to Reynolds number variations above 10^5, but that below this threshold there is a high degree of nonlinearity in the drag polar,

indicating high sensitivity to aerofoil geometry and Reynolds number variations (*Figure 2.4*). This conclusion is also presented by Gupta [8], where several aircraft configurations are tested in *XFLR5* for various Reynolds numbers and then compared with experimental results.

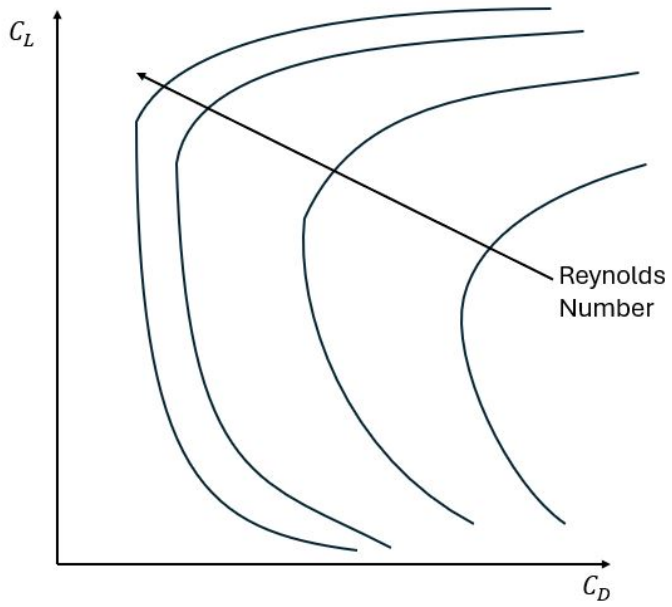

Figure 2.4: Schematic representations of drag polar variation with Reynolds number.

The authors compare experimental and computational (TURNS2D) results for various conventional aerofoils as well as thin plates in a Reynolds number range of 2×10^4 to 10^6, with the aim of studying the influence of the Reynolds number on those profiles and validating the computational software with those results. In relation to the latter, it is stated that while the simulations can generally approximate the behaviour of the curves, eddy viscosity is often overestimated, leading to less accurate results. In relation to the former, [7] conclude that, for Reynolds numbers below 10^5, a cambered thin plate provides exceptional results, to the detriment of conventional aerofoils, and that the aerodynamic characteristics of an aerofoil cannot be assumed constant.

The work of Winslow *et al.* [7] is relevant to this dissertation because the Reynolds number interval in which small-sized UAVs are expected to operate is consistent with what is presented. Under these conditions, an LSB is expected to form in the wing-fuselage interface for low angles of attack. This could significantly increase interference drag, which could be reduced with the introduction of a fairing. This topic is explored in *Chapter 2.3*.

2.2 Computational and Experimental Approaches in Drag Analysis

Although the empirical approximations provided by Hoerner [6] do offer a generally precise method for calculating the magnitude of interference drag without the need for experimental procedures, these, along with modern computational methodologies, have provided many insights into the manifestation of interference drag between the wing and the fuselage. This chapter is dedicated to the general presentation of experimental approaches of drag determination and a more detailed overview of computational approaches for the same effect. While experimental methods are not relevant in the scope of this work, having a clear perspective of how these experiments are conducted does allow for a broadened perspective, as well as a basis for comparative studies.

2.2.1 Experimental Approaches

Méheut and Bailly [9] argue that while results obtained from CFD computations are becoming more accurate, it is not yet possible to provide a reliable decomposition of the calculated drag into its components. Therefore, they build upon previous work, developing a method consisting of the formulation of profile and induced drag components in terms of flow quantities calculated directly inside the wake of a body. This original method allows for the extraction of the drag components and was validated by comparison with CFD computations and experimental wind-tunnel measurements.

The far-field approach, as employed by the authors, consists of the integration of the momentum equation inside a closed volume surrounding the model. The drag equation is written in terms of wake variables, unlike the near-field approach where the values are integrated over the model's surface. *Equation 2.3* defines the total drag of a model based on the assumptions that only the aft face of the volume contributes to total drag and considers only the upstream flow axis.

$$D = -\int_{\Sigma_1} \left[\rho\left(U - U_\infty\right)\left(\boldsymbol{V}.\boldsymbol{n}\right) + \left(P - P_\infty\right) n_x\right] \mathrm{d}s \quad (2.3)$$

where ,ρ,P,P_∞,V and U_∞ are the density, the local and upstream static pressures and velocity vectors($V = (U; v; w)$ and $U_\infty = (U_\infty.x)$). Introducing the notion of the drag Coefficient $C_D = \frac{2D}{\rho_\infty U_\infty^2 s_{ref}}$, it is possible to rewrite *Equation 2.3* in terms of the measures of the wake variables in *Equation 2.4*.

$$C_D = \frac{2}{S_{\text{ref}}} \int_{\Sigma_1} \left[\frac{T_{i\infty}}{T_i} \frac{P_i}{P_{i\infty}} \Im^{\frac{1}{\gamma-1}} \frac{U}{U_\infty} \left(1 - \frac{U}{U_\infty}\right) + \frac{1}{\gamma M_\infty^2} \left(1 - \frac{P_i}{P_{i\infty}} \Im^{\gamma-1}\right) \right] \mathrm{d}s \tag{2.4}$$

where M_∞, γ, P_i, $P_{i\infty}$, T_i and $T_{i\infty}$ are the upstream Mach number, the specific heat ratio, the local and upstream stagnation pressures and temperatures, respectively. $\Im$ is defined as:

$$\Im = 1 + \frac{\gamma - 1}{2} M_\infty^2 \left(1 - \frac{V^2}{U_\infty^2} \frac{T_{i\infty}}{T_i}\right) \tag{2.5}$$

While these equations allow for the determination of the total drag of a body, they do not provide any insight into the components of this force. The following general formulations for the profile and induced drag components will allow for the determination of drag for different configurations of aircraft, therefore allowing an analysis of interference drag from wake measurements.

The authors proceed to analyse and compare several different methodologies for drag breakdown from wake flow measurements based on the previous equations, culminating in a general methodology applicable to any three-dimensional, compressible or incompressible flow. In this dissertation, the need for a drag breakdown in compressible flow is not relevant, since UAVs fly at rather low speeds ($M <= 0.2$). With this in mind, the formulation presented by Maskell [10] and summarized by the authors does provide a very good approximation of a drag breakdown at low Mach numbers.

Maskell [10] introduces the total pressure field expression with what the author calls an artificial velocity U^*. They also define a blockage velocity u_b, which is a correction for the confinement effect. By working *Equation 2.3*, the author arrives at *Equation 2.6*, which represents the profile drag coefficient of a body.

$$C_{\text{Dp}}^{\text{Maskell}} = \frac{2}{S_{\text{ref}}} \int_{\text{wake}} \left(\frac{P_{t\infty} - P_t}{\rho_\infty U_\infty^2}\right) \mathrm{d}s + \frac{1}{S_{\text{ref}}} \frac{\rho}{\rho_\infty} \int_{\text{wake}} \left(\frac{U^* - U}{U_\infty}\right) \left(\frac{U^* + U - 2\left(U_\infty + u_b\right)}{U_\infty}\right) \mathrm{d}s \tag{2.6}$$

Taking into account that the induced drag is a result of the change in momentum of the cross-sectional flow, Maskell [10] introduces scalar functions ϕ and ψ for the cross-sectional velocities v and w, which are, respectively, related to the trailing vorticity ζ and

the velocity gradient σ through Poisson equations. This results in *Equation 2.7*, describing the induced drag coefficient of a body.

$$C_{\mathrm{Di}}^{\mathrm{Maskell}} = \frac{1}{S_{\mathrm{ref}}} \frac{\rho}{\rho_\infty} \int_{\mathrm{wake}} \frac{\psi\zeta}{U_\infty^2} \, \mathrm{d}s - \frac{1}{S_{\mathrm{ref}}} \frac{\rho}{\rho_\infty} \int_{\Sigma_1} \frac{\phi\sigma}{U_\infty^2} \, \mathrm{d}s \quad (2.7)$$

Maskell's [10] model does have a few limitations that Méheut and Bailly [9] point out. It must be noted that this formulation, theoretically, can be applied to compressible flow. This is the case because the artificial velocity U^* is consistent and intended to be used taking into account Trefftz-plane assumptions. This use does imply that the survey plane must be a Trefftz plane, which is very limiting, especially if the survey plane is not far away from the model. Therefore, the application of this model to compressible flow cannot guarantee a reliable evaluation of drag at high Mach numbers. The reason behind this conclusion is that Maskell [10] does indeed base his model on the total pressure field of the wake, which is identical to the stagnation pressure field in incompressible flow. In compressible flow it is different, resulting in less reliable values for drag.

2.2.2 Computational Approaches

In this dissertation, the information needed for the calculation of interference drag will be solely acquired through CFD simulations utilising the commercial software *ANSYS Fluent*. The software allows the user to solve a particular flow field in its entirety, providing the information needed for drag calculations. The precision of the data is highly dependent on the setup of the simulation. For example, the turbulence model utilized, the mesh and its properties, the flow parameters, boundary conditions, etc. are all of importance when undertaking CFD simulations. In this subsection, only the turbulence models will be discussed, since these are the base of any simulation and the main constraint when it comes to precision. The general methodology of CFD simulations is explored in *Section 2.4*.

Considering most small-sized commercial UAVs fly in the transition regime between laminar and turbulent flow, the simulations must make use of a model that can correctly accommodate all the structures and intricacies of turbulent flow, such as wing tip vortices, separation, boundary layer phenomena, etc.

Wilcox [11] brings a new approach to how the $k - \omega$ method works the boundary layer, adding to the ω equation production and dissipation terms analogous to the k equation, bringing the results much closer to measurements near the wall. The great limitation was, still, the strong adverse pressure gradient that destabilised the model. In his work, the author admits that using the Boussinesq approximation (stress is proportional to strain) is insufficient in predicting the anisotropy of the normal stresses and the curvature of the

flow streamlines. Even so, the results presented are superior to the $k - \varepsilon$ model. Further work resulted in the addition of several terms to the original method of Wilcox, including a "cross-diffusion" and "stress limiter" modification that makes the eddy viscosity a function of k and ω. These last modifications to the method increase its robustness without degrading the results at all. In fact, in free-shear flow, the results are closer to the measurements [12]. More recently, developments of the $k - \omega$ model include the BSL $k - \omega$ and SST $k - \omega$ models by Menter [13], and the *GEKO* model commercialised by *Ansys*, also developed in collaboration with Menter.

Wilcox [14] presents a summary of several turbulence models, and how their advantages and limitations condition their use in industrial and engineering activities. The author begins by stating that the difficulty of developing a general turbulence model, besides the obvious limitation of computational resources, lies in the necessity for said model to contemplate both large and small scale structures, as stated before. Since solving the Navier-Stokes Equations (NSE), except for very low Reynolds and specific cases, is practically impossible, models for the simplification of the NSE equations allow to save time and resources at the cost of precision.

The author explains, through experimental and computational results, that zero equation models (algebraic models) provide satisfactory results for attached flow, but are entirely unreliable when simulating detached flow. One equation models, on the other hand, such as the Spallart-Allmaraz model, when well conditioned to the problem at hand, provide good results in an engineering context. However, they fail to accurately represent more complex flows. Wilcox [14] goes on to present and validate two-equation models, providing insights into how the modelling of turbulence is conducted: one equation representative of the turbulent kinetic energy and another representative of a second turbulence scale.

The main two equation models compared by Wilcox are the $k - \varepsilon$ and the $k - \omega$ models. The main point made by the author is that the $k - \varepsilon$ model tends to overestimate the spreading rate by up to 40% in some cases, with the estimation for the friction coefficient also overestimated by 30%. In these conditions, the $k - \omega$ model performs much better, with only a relative error of 3.5% to the measured data. When it comes to detached flow, the $k - \varepsilon$ displays optimistic behaviour for the reattachment of the flow, triggering several modifications to the model. By contrast, the $k - \omega$ model depicts the measurements accurately without any kind of modifications.

For this reason, the turbulence model used in this dissertation will be the $k - \omega$ model, as it provides the best results in terms of turbulent structure simulation and result precision.

2.3 Previous Studies on Wing-Fuselage Interference Drag

As aircraft become increasingly efficient, interference drag has become an ever more relevant component of overall drag. Over the last century, several wind tunnel experiments have been conducted, as well as numerical approximations and CFD analysis, aiming to understand and reduce interference drag in aircraft. This chapter explores these strategies, provides an overview of their methodologies and results, and compares them with each other.

2.3.1 Experimental Studies

Experimental studies on interference drag are conducted almost exclusively in wind tunnels because of their flexibility and quickness. Moreover, they allow for the gathering of data for several models under uniform conditions and with a controlled error.

Klein [15] experiments with different fillet fairings for an existing aircraft. The experiments were carried out in a large-scale wind tunnel, with the model spanning $18m$ across. Total and static pressure measurements were taken on the model surface, and wake measurements were also available for several angles of attack. The fairings were constructed of wax with a kerosene finish. Although the wind tunnel's operating Reynold number was $2,1 \times 10^6$, the fairing design principles can still be applied here, since, as explained below in this chapter by Maughmer [16], the effects of fairings are positive for both high and low Reynolds numbers. The fillet fairings were designed with a constant radius of 15% of the root chord and the one that provided the best results for a low-wing configuration had a small nose and the same radius at the trailing edge, resulting in an elongated fairing towards the back of the fuselage (*Figure 2.5*). For high-wing configurations, it was stated that fairings do not make a large difference in drag. In fact, it increases slightly. The fairing utilised for this configuration had a 20% root chord radius and was tapered at the trailing edge. The main conclusions reached by the author are that the aerodynamic disadvantages of a low-wing configuration can be almost completely eliminated by a proper fairing design, and that the maximum lift coefficient of the isolated wing can be achieved in either a low or high-wing configuration. The difference in drag between these both configurations with a fairing can be neglected. As for fairing design, Klein states that the minimum drag of the wing-fuselage interface can be reduced by making the fillet at the leading edge as small as possible.

Jacobs and Ward [17] test two hundred and nine different aircraft configurations, varying vertical and longitudinal position, as well as wing incidence and angle of attack (AOA) at several Reynolds numbers. The major variables in this experiment were the wing planform and the aerofoil section, the cross-sectional shape of the fuselage, and the vertical position of the wing. The relevant minor variables were fillets in the wing, longitudinal position of the fuselage, and longitudinal position of the wing. Although most of the tests

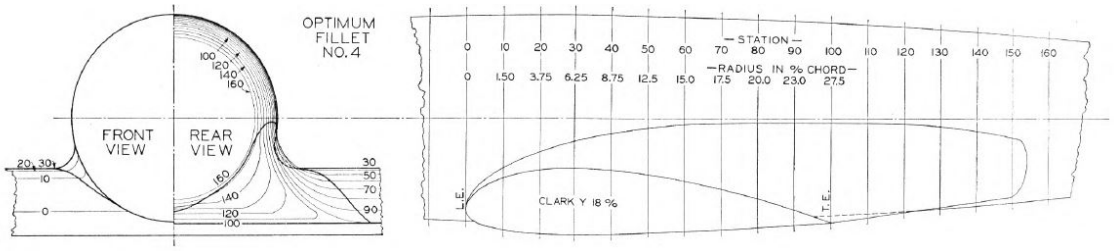

Figure 2.5: Lines of the optimum fillet. Adapted from Klein.

were performed at 3.4×10^6 Reynolds, an additional experiment was performed at 1.4×10^6 Reynolds to determine the maximum lift for most combinations. The authors state that due to the nature of the tests conducted, the results suffer from cumulative errors. These are derived from the supports used to hold the models in place and also from corrections done to the models at high AOA when the wing is disconnected from the fuselage. In order to avoid misinterpretations of data due to induced drag, especially at high AOA and when induced drag has different effects in different combinations, an effective profile-drag coefficient is introduced, which represents the difference between the total drag coefficient and the minimum induced drag coefficient. The explanation of "interference burble", or separation of the flow over the interface, is explored, with its relevance increasing with the AOA of the aircraft, as is expected. The authors also consider a sudden increase in lift where the wing meets the fuselage, which they consider as an increase in local chord, much like what Hoerner [6] calls α flow. They explain that, for high AOA, the fuselage carries more lift than the section of the wing it encloses, leading to a virtual increase in AOA at the wing root. This boundary layer interference causes premature stalling, which again increases the virtual AOA in the wing profile, and so on. Regarding the vertical position of the wing, it is stated that a high-wing configuration presents an interference drag that is much higher than that of a mid-wing configuration. In lower positions of the wing, close to the underbelly of the fuselage, interference drag becomes high again. It is explained that the angle at which the wing meets the fuselage, if it is acute, greatly influences the interference drag in an adverse way. Having also presented configurations that donned interface fillets, it is observed that the main advantage of these structures is to delay flow separation in the interface, with all types of fillets used increasing interference drag slightly.

Hoerner [6] establishes the aforementioned empirical correlations that translate experimental findings into mathematics. With respect to interference drag, Hoerner's experiments, like those of his successors, indicated that the position of the wing on the fuselage influences interference drag substantially. The author states that, for zero-lift conditions, the interference drag of the wing-fuselage interface (mid-wing configuration) decreases with the distance from the nose of the aircraft. Moreover, Hoerner states that the results of his experiment indicate that, in zero-lift conditions and for a mid-wing, interference drag may be lower than the combined drag of the isolated components, resulting in positive interference. The explanation provided is that connecting the wing to the fuselage

reduces the total wetted area of the wing, resulting in a lower total drag at the interface. It is also stated that, while interference may have a positive effect for zero-lift conditions, the phenomenon of α flow leads to an increase in induced and parasitic drag along the root of the wing at the interface, which compensates for the gains from positive interference.

Kubendran, McMahon and Hubbartt [18] provide a summary explanation of the phenomena behind interferences, stating that there are two vorticity-generating mechanisms in a wing-fuselage interface: the skewing of the initial turbulent boundary layer, generating a streamwise vorticity in the interface; the "Horseshoe" vortex common in flow separation (*Figure 2.6*). The experiment consisted of studying the interference drag of a interface between a simetrical elliptical profile in zero-lift conditions and a flat plate. This configuration simulates a simetrical wing profile connected to a circular fuselage of much greater radius compared to the wing thickness. Data was gathered in a wind tunnel through static pressure probes and hot-wire anemometers. The wind tunnel was operated at a Reynolds number of $9,4 \times 10^5$. The authors worked the data in relation to total momentum deficits within the interface, and concluded that, under these conditions, the interference effect was positive, i.e. drag was reduced relative to both components taken in isolation.

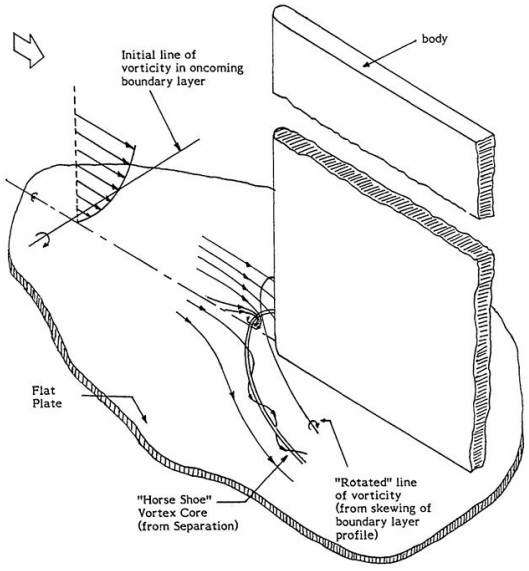

Figure 2.6: Schematic of the flow in a wing-fuselage interface. Adapted from Kubendran.

Bernstein and Hamid [19] explore the use of a strake-shaped interface fillet in low-speed aerodynamics (*Figure 2.7*). The authors conducted their research on an Airbus A320 variant at an average Reynolds number of 1.56×10^6 and for several AOA. Measurements of mean velocity fields were made in the vicinity of the leading edge via a purpose-built yaw meter and an "X-wire" anemometer, which was also used downstream of the trailing edge. These measurements also allow for calculations of five Reynolds stresses. The results obtained were somewhat inconclusive. It was determined that the fillet moderated the increase in sectional drag as the wing root is approached only to a small extent. However, the overall flow is considerably altered, with the characteristic horse-shoe vortex also re-

ported by Kubendran [18] much less defined; it was found that the turbulence intensity decreased over all AOA, but that the turbulent area was spread over a larger proportion of the wing. Bernstein and Hamid finally stated that a well-optimised strake-shaped fillet for cruise conditions can reduce the peak turbulence intensity associated with these kinds of interfaces; it remains unclear, however, how this fillet influences total drag values.

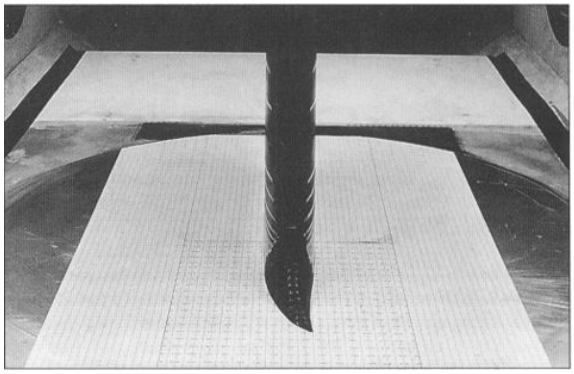

Figure 2.7: General view of the swept wing-plate model mounted in the low speed wind tunnel. Adapted from Berinstein.

Maughmer *et al.* [16] conduct experiments on three leading edge blending geometries, concluding that a forward, sharpened bleeding edge-shaped linear fairing can reduce interference drag in lift conditions up to 5% across the drag polar of the tested sailplane (*Figure 2.8*). The authors tested said geometries in small-scale ($1/4$ scale) models for flow visualisation and force-balance. These models were symmetrical about the fuselage and had wings truncated at 40% of the full span. The wind tunnel operated at a Reynolds number of 4×10^5 for a test section of $1,2 \times 1,5m^2$ of area. Pressure measurements were taken in a $1/7th$ scale model in the same wind tunnel operating at a Reynolds number of $2,5 \times 10^5$. The results presented by the authors indicate that a low-thickness ratio is desired at the root of the wing, which is achieved by artificially extending the leading edge through the use of the fairing. They also show that, according to their research, these fairings are beneficial in both laminar and turbulent flow, becoming more effective as the Reynolds number decreases (viscous effects become dominant).

Kentfield [20] conducts experimental wind tunnel research on several configurations of wing position and four different models of fuselage, with three of them of the short pod type. Although the author focuses on Outboard Horizontal Stabilizer (OHS) configuration aircraft, this work focuses specifically on wing-fuselage interference drag. Tests are carried out with a variable configuration setup within a $1,37 \times 0,76m^2$ test area (within a Reynolds number interval of 6×10^4 and 3×10^5) where the horizontal and vertical wing positions are adjustable, as well as the fuselage vertical orientation (this allows for high or low-wing testing) and wing incidence. The wing is not swept or tapered and the wind tunnel functions in low velocity, free-jet configuration. The variables in this work are the distance h between the fuselage and the wing and the position X between the fuselage nose and the quarter-chord position of the wing. The measurements were presented in the

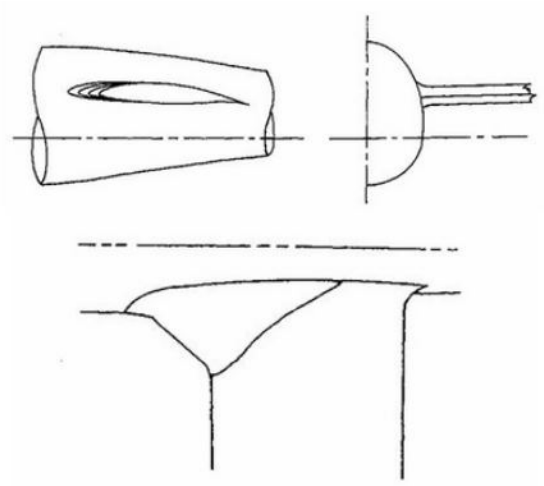

Figure 2.8: Profile, front and planform view of wing/fuselage integration geometries. Adapted from Maughmer.

form of a drag balance between the measured drag coefficient of the configuration and the free-flow fuselage drag coefficient only. Kentfield notes that the wing-fuselage pressure field coupling influences drag characteristics of aircraft, although this phenomenon is less relevant in long fuselages, such as those found in conventional configuration aircraft. The author states that, for low-wing aircraft, positive interference is only achievable for very forward positions of the wing. In more common positions, a low-wing aircraft produces much higher interference, allegedly because of the mutual influence of both components' pressure fields. As for the high-wing configuration, it is stated that, for conventional wing positions, interference effects are minimised, and in some cases even favourable.

2.3.2 Computational Studies

The computational efforts led by various researchers to understand and develop strategies to reduce interference drag are significant. Unlike the works discussed above, where the geometry and position of the fairings is essentially trial and error, the following research is based on iterative optimisation, delivering the best results for the expressed constraints.

Song and Lv [21] use free-form design optimisations to produce a fairing that reduces total drag for a given lift coefficient. The methodology employed by the authors relied on the use of non-uniform rational B-splines, which allow for the bounded control of parameters in two levels: a coarse set to capture physical and structural constraints and a refined set that controls local details. This reduces the dimensionality of the optimisation while allowing flexible and realistic shapes to be built into the parametrisation without needing to handle violations explicitly. Due to each fairing needing a full CFD simulation, the authors used a Kriging surrogate model to approximate aerodynamic performance. This model is trained on sample designs. The optimised fairing achieved a reduction in drag relative to the

baseline fairing model and suppressed flow separations in the wing-fuselage interface. In addition, it reduced the characteristic intensity of the horseshoe vortex, improving flow attachment, and increasing efficiency. The two-level parametrization proved effective and embedding the design constraints in the B-splines eliminated unfeasible designs, reducing unneeded CFD simulations.

Matos and Marta [22] develop a method for designing the optimal shape of the intersection region between the wings and the fuselage of a MALE UAV using gradient-based methods and free-form deformation techniques. The authors tested several deformation strategies for both the wings and the fuselage, allowing them to determine which combinations of parameters yielded the best results individually and together. The base model selected for this work was the *Tekever ARX*, a $12m$ span UAV developed by *Tekever UAS* (*Figure 2.9*).

Figure 2.9: Test case UAV: Tekever ARX. Current detailed design. Adapted from Matos.

Simulations were performed for an AOA ranging from $-4°$ to $12°$ to map several operating conditions. For an AOA of $6°$, the optimisation algorithm proved to be very effective, achieving a reduction of 1.85% in total drag. However, the authors state that this analysis lacks an off-design performance perspective. Thus, the authors introduce a second operating point of $0°$, representative of cruise flight conditions. This off-design analysis provides good results in drag reduction for both operating conditions while maintaining critical AOA aerodynamic characteristics. Geometrically, the optimal configuration involves a constriction of the fuselage throughout the wing chord, and a slightly high and forward wing (*Figure 2.10*).

2.4 CFD Methodologies

The results obtained in CFD simulations vary widely depending on the simulation setup, the turbulence model utilised, and the boundary conditions imposed. This section will explore some commonplace practices that improve the reliability of said results, exploring subjects like mesh independence, the solver utilised, and the prediction of transition phenomena.

One of the most important aspects of CFD simulations is the geometry for which the flow

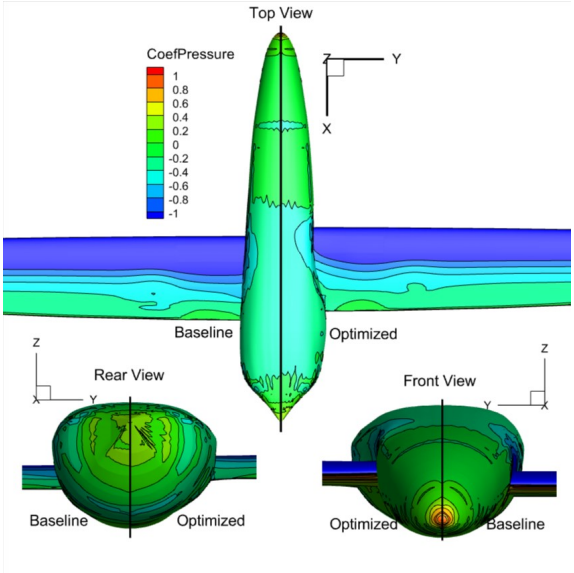

Figure 2.10: Combined fuselage and wing multi-operating-point optimization: comparison of pressure coefficient between baseline and optimal shape. Adapted from Matos.

properties are calculated. Assuring that the geometry is in line with the conditions and limitations of the CFD setup is imperative for the fidelity of the results. One such example that is relevant in the context of this dissertation is presented by Van Dam [5]. The author explains that the finite thickness of an aerofoil's trailing edge leads to modelling problems related to the Kutta condition, which degrades results substantially. The author explains that solving this issue relies on "cutting" the smooth trailing edge, making it sharp, and then normalising the result until the maximum thickness ratio is achieved. They state that this change in geometry significantly alters drag results (about 15% in their case), which becomes even more of an issue if other variations of geometry are considered, for example, in fuselages or engine nacelles.

The mesh size in CFD simulations is another factor that significantly influences the fidelity of the results. Although computational performance has increased in the last few decades, the need for a denser mesh is still outweighed by the need for faster simulations. Van Dam [5] presents two different methods for predicting the independence of the mesh but concludes that for a reasonable difference in 0.5 drag counts, in their specific example, the mesh would require 15×10^9 billion cells, which is impracticable. One workaround presented by the author and based on previous work is the concentration of elements near the surface of the body, allowing for the precise calculation of near-field phenomena without losing much precision in far-field effects. While not ideal, this does allow for substantial reduction of the number of elements in the mesh, speeding up simulations and saving resources.

The selection of the solver methodology is also relevant for the fidelity of the results. Taking into account the previous paragraph, it is important to note that the results should be independent of both the mesh size and the solver utilised. More often than not, the re-

sults vary more over solvers available rather than mesh size. This happens because some solvers have limitations and corrections that alter how the flow is evaluated and solved, altering the end result. The level of convergence of the results also influences their precision. While it is important to consider that low convergences intervals lead to more precise results, it must be taken into account that the higher the convergence level the higher the computational and time costs.

The prediction of the flow transition and the development of flow conditions over time is always dependent on the model used for turbulence, as per *Chapter 2.2*. While simpler models may require a transition position specified as a percentage of local wing chord [5], modern implementations of applicable turbulence models, such as those provided by *ANSYS* and used in this dissertation, already have these phenomena considered.

In summary, these factors must be taken into account for building the CFD setup for a simulation. Even though some of them, such as the mesh size or the turbulence model, may require more attention or effort than other, all of them are equally relevant for the precision and fidelity of the results.

Chapter 3

Methodology

The computational method used in this study follows the formal organization presented in *Figures 3.1 and 3.2*, covering the entire process from geometric definition to numerical analysis.

Figure 3.1 illustrates the geometric design process starting with wing planform and aerofoil definition, with subsequent refinement in *XFLR5*. The fuselage geometry was manually defined in *CATIAV5* so that both parts could be integrated into a single assembly. The assembled configuration was configured to the given angle of attack and exported to the *ANSYS* environment, where it is properly processed prior to mesh generation.

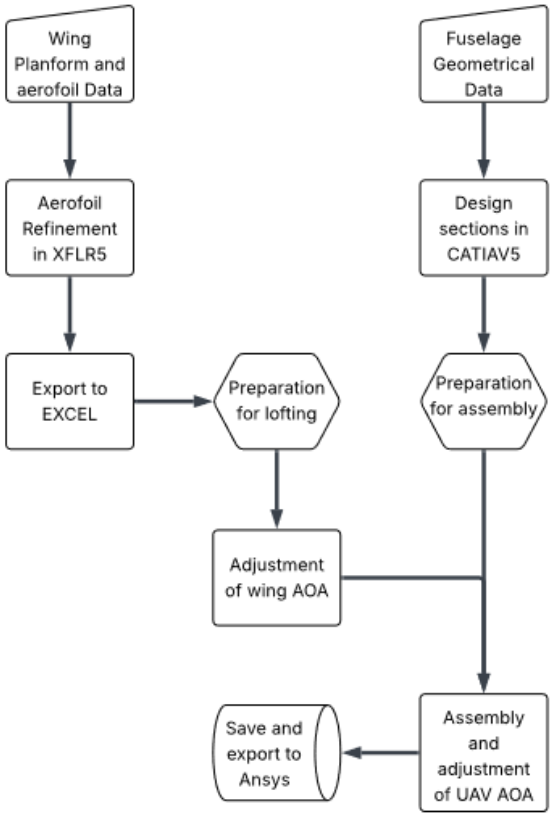

Figure 3.1: Diagram representing the geometrical modelling process of the methodology.

Figure 3.2 illustrates the methodology used within *ANSYS* to execute the simulations. The process began with the import and repair of the computer assisted designed (CAD) geometry in *ANSYS Discovery*, followed by the definition of the body of influence and control volume. Mesh generation, boundary conditions and solver settings were defined

in *ANSYS Fluent*. Simulations were run as steady state, with appropriate discretization schemes and standard convergence criteria to ensure result fidelity. Post-processing consisted of the calculation of aerodynamic coefficients, with which the subsequent analysis of turbulence model fidelity was conducted. The two diagrams synthesise the methodology discussed below into a consistent and reproducible process that couples geometric modelling and computational analysis in a consistent manner.

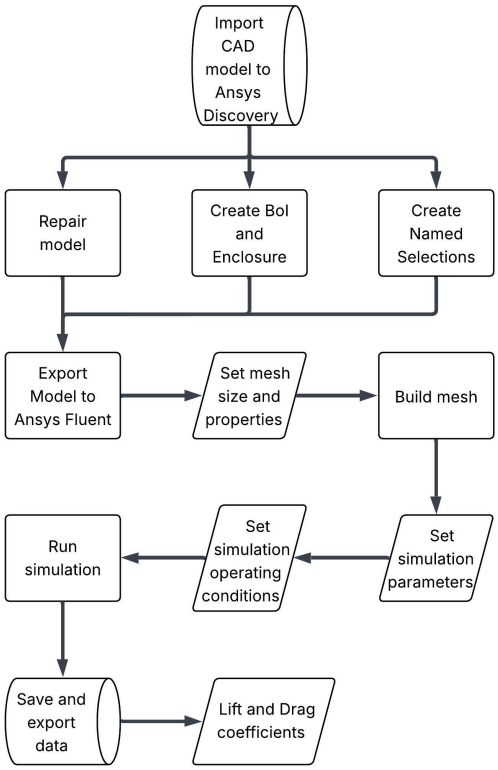

Figure 3.2: Diagram representing the CFD simulation process of the methodology.

3.1 CFD Turbulence Model Validation

The validity of the results achieved in this work depends on the validity of the turbulence model used. Therefore, and in accordance with Chapter 2.2, an attempt is made to validate the $k - \omega$ SST turbulence model by comparison with already existing experimental work on low-Reynolds number interference drag between the wing and fuselage interface.

The case-study selected for this validation is obtained from *The Interference between the Body and Wings of Aircraft* [23], in which the drag and lift coefficients of several combinations of wing and fuselage are analysed in a wind tunnel. This work was chosen for the conditions under which the analysis is done and for the variety of cases studied. In the next sections, the validation process is presented and analysed, ending with positive results that support the use of selected turbulence model.

3.1.1 Geometry Definition

The geometric dimensions and representations of the bodies used by the authors are described and presented in their entirety, allowing for their replication. The authors analyse three different aerofoils (RAF-15, USA-27, and Gottingen-387) although only the medium-thickness USA-27 is considered in this validation. The dimensions of the wing are also described, with a chord of $76.2mm$ and a span of $457.2mm$, resulting in an aspect ratio of six. The geometry of the fuselage is represented as an orthographic projection, with the longitudinal and vertical positions of the wing well defined. The models used by the author are considered smooth, that is, very low to no roughness. The combination of the wing and the fuselage will henceforth be referred to as the "structure". *Figure 3.3* represents the end goal fuselage geometry to model.

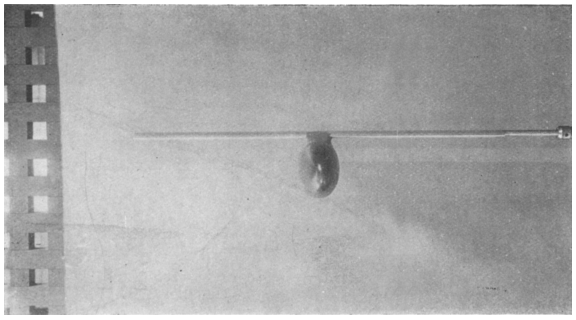

Figure 3.3: Front view of set up with fuselage A showing fairing. Adapted from Parkin.

CAD modelling of the structure begins with the *2D* definition and refinement of the USA-27 aerofoil in *XFLR5*. The initial representation of the aerofoil was acquired from an online aerofoil database [24] and then transferred to the *Direct Foil Design* Module of *XFLR5* [25], where the number of points that constitute the spline was increased from 100 to 200 using the *Refine Globally* function. The result was then exported to *Excel*. At this point, the aerofoil has a chord of one unit of length, which will be treated as one millimetre in this validation. Therefore, it must be scaled to the correct chord length by multiplying each coordinate by $76.20mm$. Utilising *CATIAV5*'s *GenerativeShapeDesign Excel* file, it is possible to define and loft a wing with the desired geometric characteristics, which is then imported into an open *CATIAV5* part and ready for use (*Figure 3.4*).

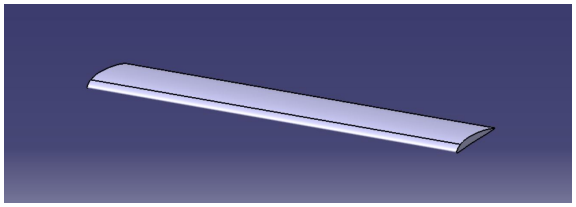

Figure 3.4: Graphical representation of wing surface in *CATIAV5*.

The geometry of the fuselage is achieved in an entirely different manner. Using the orthographic projection provided in the article by the authors, it was possible to draw the

outlines of the fuselage by manually creating splines that follow the contour of the outlines and then create three sections along the body that ensure the relevant tangency constraints. These sections were then joined using the *multi-section surface* function using the outlines as guidelines for the lofting. The nose of the fuselage was modelled using the *fill* function, respecting all relevant tangency constraints. The surface model was then scaled to the correct length of $350.87mm$ using the *scaling* function (*Figure 3.5*).

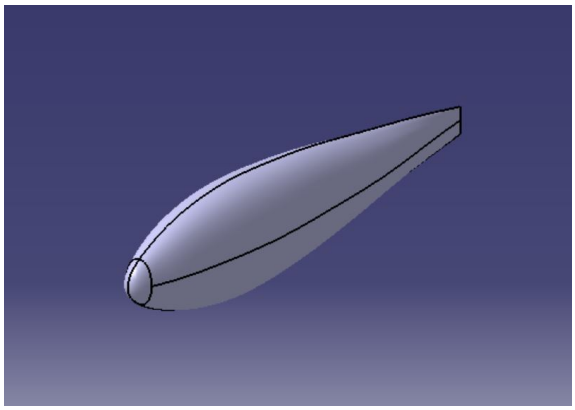

Figure 3.5: Graphical representation of fuselage in *CATIAV5*.

With both components of the structure built, the wing was positioned longitudinally as instructed in the orthographic projection with an AOA of 2° (*Figure 3.6*). Two main setups were considered during this validation: mid-wing and high-wing. For the mid-wing setup, the wing was vertically positioned tangentially above the fuselage chord line, and for the high-wing setup, the wing was vertically positioned tangentially above the fuselage surface. The AOA of the structure was then varied relative to the fuselage chord line as required for analysis.

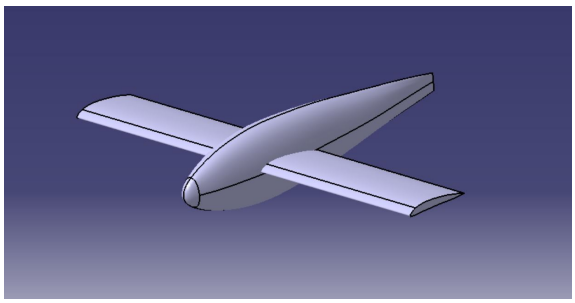

Figure 3.6: Graphical representation of the structure in *CATIAV5*.

The methods utilised for building the geometry ensure that the geometric accuracy of the wing is quite high, but the same cannot be said for the fuselage. Manually fitting the splines that define the loft leads to small cumulative inaccuracies along the fuselage chord line that can influence the airflow over the body. Furthermore, the exact body shape cannot be achieved due to the lack of intermediary section representation on the orthographic projection. The result was a fuselage with curvature inconsistencies and a small face at the trailing edge, instead of the represented vertical “knife” edge. All these differences

between the article and the validated geometry will lead to differences in the results.

3.1.2 Preparation of Model for CFD Simulations

Setting and computing the simulation results require a cleaned and prepared model in order to avoid software errors and ensure the validity of the results. This preparation was done using *Ansys Discovery* [26].

The structure was uploaded into *Ansys Discovery* and all geometry errors were fixed using the functions provided in the "Repair" tab. The model was then enclosed, reaching out $300\ mm$ in all directions, except for the posterior face of the enclosure, which was extended $1000\ mm$ away from the fuselage bleeding edge. The model was then cut vertically along the longitudinal axis, creating a symmetry plane in the model. The reason for this is savings in computational resources and time without loss in accuracy. The geometry was repaired again, and a box-style body of influence was created around the fuselage, spanning one third of the wing chord in every direction, with the exception of the posterior face, which extended until the end of the enclosure. All geometric elements were suppressed for physics, with the exception of the enclosure and the body of influence.

Named selections were then created for each boundary region in the model, which are enumerated below and represented in *Figure 3.7*:

1. "Inlet" - Anterior face of the enclosure;
2. "Outlet" - Posterior face of the enclosure:
3. "Symmetry´´ - Face where the model was cut;
4. "No shear wall" - Remaining three faces of the enclosure;
5. "Structure" - All the faces that build the structure geometry.
6. "BoI" - Body of influence.

The model is now ready to be imported into *Ansys Fluent*.

3.1.3 Boundary and Operating Conditions

The operating conditions under which the wind tunnel tests were carried out are essential for the replication of the results and the validation of the model. Apart from the temperature at which the tests were conducted, all necessary boundary conditions were specified.

The air velocity used by the authors was $40\ fps$ or $12.192\ m/s$. Although the exact temperature is not stated, there is reference to the latter half of the summer of 1927, which is considered in this work to be August 1927. From historical documents, the average

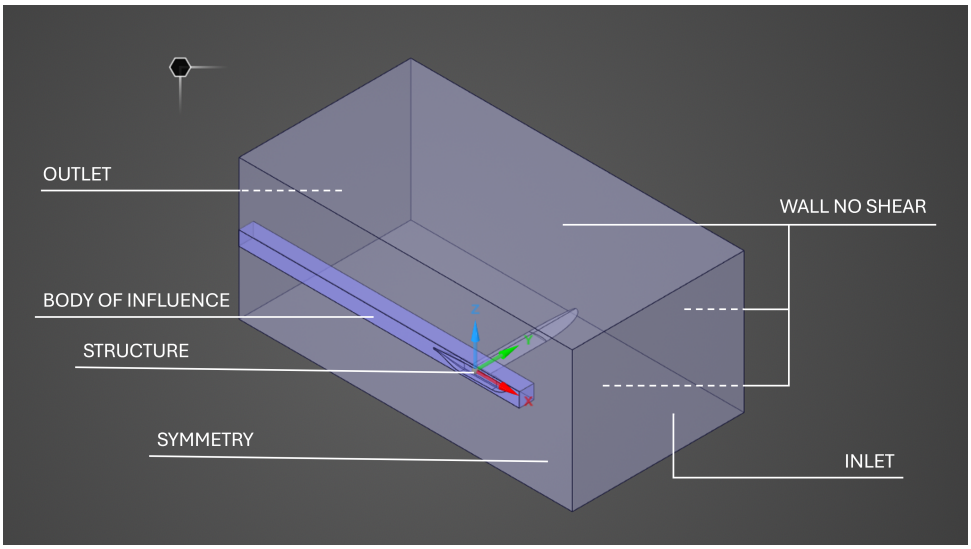

Figure 3.7: Representation of simulation setup with named selections.

temperature in Toronto was $18°C$ [27]. At this temperature, the kinematic air viscosity is $1.803 \times 10^{-5}\ m^2/s$. The reference area used in the simulations was that projected on the xy-plane, which was calculated by *Ansys Fluent* as $0.2105\ m^2$. The absolute operating pressure used was $101325\ Pa$ and the gauge pressure is $0\ Pa$. These values are the same for every simulation. The Reynolds number was calculated with the wing chord, resulting in a Reynolds of roughly 5×10^4. Other unmentioned reference values were set as default by *Ansys Fluent*.

The boundary conditions for the simulations were set based on the imported Named Selections:

1. "Inlet" - Velocity inlet boundary condition of $12.192\ m/s$ and 1% turbulence intensity;

2. "Outlet" - Pressure outlet boundary condition of $0\ Pa$ gauge pressure and 1% turbulence intensity;

3. "Symmetry" - Symmetry boundary Condition

4. "No shear wall" - Wall boundary condition with specified shear of $0\ N/m^2$ in every orthogonal direction;

5. "Structure" - Wall boundary condition

Other unmentioned boundary condition values were set as default by *Ansys Fluent*.

3.1.4 Mesh Generation

The generation of the mesh was performed using the "Watertight Geometry" workflow, where predefined functions to generate the mesh are specified and executed in order.

3.1.4.1 Mesh Strategy and Refinement

At low Reynolds numbers (e.g. 5×10^4), airflow is highly sensitive to disturbances, making it prone to early transition. As a result, resolving the boundary layer with high accuracy is essential, which requires a very fine surface mesh. Additionally, accurately capturing the wake development is crucial for reliable computation of aerodynamic quantities.

The meshing strategy, therefore, focuses on generating a fine surface mesh over the geometry and within the body of influence. The smallest mesh elements must be appropriately sized to resolve critical flow features, particularly within the boundary layer and wake.

Following the mesh workflow in *Ansys Fluent*, the geometry is imported and two local sizings are added. The first sizing of $0.01m$ is added to the structure surface and the second of $0.5m$ added to the body of influence. The surface mesh is then generated with a minimum size of $0.01m$ and a maximum size of $0.032m$. For the following function, "Describe Geometry", the first option is set to "The geometry consists of only fluid regions with no voids" and the following options are set as default. "Update Boundaries" and "Update Regions" are checked for mismatch and corrected if necessary. The "Improve Surface Mesh" function is then added to the workflow, and is updated with a minimum orthogonal quality of 0.55. Boundary layers are then added following the last-ration formulation, with 12 layers, a transition ratio of 0.272 and a first height of $0.0001m$. Lastly, the Volume Mesh is generated using the Poly-Hexcore formulation and default values.

This meshing workflow was used in all validation cases, ensuring that the respective results are comparable between the article and themselves.

3.1.4.2 mesh Independence Study

To ensure that the simulation results are not dependent on the mesh size, a mesh independence study is performed. For this validation, the structure mentioned before was used. The study was done by reducing mesh size until the results no longer depended on it. Three sizes were tested for the smallest surface element length: $0.005mm$, $0.001mm$, and $0.0001mm$. The simulations for each case were done according to *Section 3.1.3* and the results are presented in *Table 3.1*.

The results obtained were then compared in terms of relative error and it is noticeable that the difference between values decreases with mesh refinement. A relative error analysis between all cases was performed to quantify this decrease and validate this independence

Table 3.1: Lift and Drag coefficients of structure for three different mesh sizes.

Smallest element, [mm]	C_L	C_D
0.005	0.343941	0.050375
0.001	0.36059	0.032238
0.0001	0.361374	0.031123

study (*Table 3.2*). It is clear that the difference in results from $0.001mm$ to $0.0001mm$ is negligible, therefore this is the smallest element size to be used for the rest of this validation.

Table 3.2: Relative error analysis of the results for each mesh size case.

		Smallest element size, [mm]		
	Lift coefficient	0.005	0.001	0.0001
Smallest element size,[mm]	0.005			
	0.001	4.84%		
	0.0001	5.07%	0.22%	

	Drag coefficient	0.005	0.001	0.0001
Smallest element size,[mm]	0.005			
	0.001	36.00%		
	0.0001	38.22%	3.46%	

3.1.5 Simulation Setup

3.1.5.1 Settings

The setup for the simulations is straightforward considering all the variables already discussed.

The process begins with checking the mesh for any errors and checking its quality, which has already been deemed acceptable by the meshing process. The CFD model used was the $k-\omega$ SST model, with the low-Reynolds Correction and gamma-algebraic built-in transition model options checked. Furthermore, and as required by these options, additional Production Kato-Launcher and Production Limiter options were also checked. All constant values of the model were left as default by *Ansys Fluent*. The whole domain was treated as a fluid and the boundary conditions were applied and checked as per *Section 3.1.3*.

As for the simulation methods, the pressure-velocity coupled scheme was used and the spatial discretization was treated with second-order equations. The Gradient discretization was done using the Least Squares Cell Based method. The solutions controls, or relaxation factors, were left as default. Two report variables were created for the lift and drag coefficients of the model, which relate only to the structure and are averaged over 75 iterations. The coefficients are aligned with their respective axes.

The initialisation is hybrid, and the simulation is checked before being started. It runs for five hundred iterations. The resulting coefficients are then averaged from the last 100 iterations and registered. It has been noted that all the simulations have stabilised around 125 iterations.

3.1.6 Simulation Cases

3.1.6.1 Case Descriptions and Variations

To validate the CFD model, several cases studied by Parkin [23] have been simulated with two main structure configurations: a high-wing configuration and a mid-wing configuration.

The mid-wing structure is the same that was utilised for the mesh independence study. Three cases were analysed for this model, in reference to the fuselage AOA: $0°$, $4°$, and $8°$. The high-wing structure was modelled from the previous structure by pulling up the wing to the edge of the fuselage until the trailing edge of the aerofoil touched the fuselage surface. The same three AOA were analysed. *Figure 3.8* presents the right lateral view of all variations for each model.

The six models used in this validation were constructed using the same methodology as described in *Section 3.1.1*.

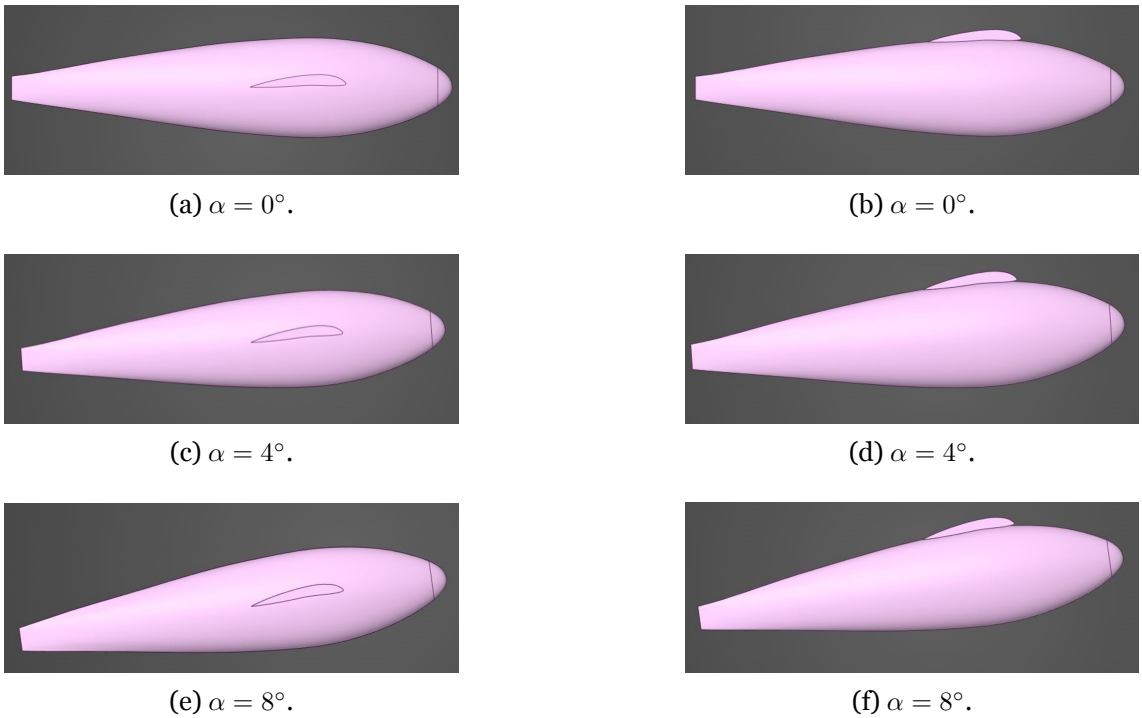

(a) $\alpha = 0°$. (b) $\alpha = 0°$.

(c) $\alpha = 4°$. (d) $\alpha = 4°$.

(e) $\alpha = 8°$. (f) $\alpha = 8°$.

Figure 3.8: Representations of angles of attack in mid-wing model (left) and high-wing model (right).

3.1.6.2 Results and discussion

The methodology used to analyse the six cases was the same as that used in the mesh independence study. The results show that even taking into account unknown variables not mentioned in the work of Parkin [23] and irregularities in the geometric models used, the $k-\omega$ SST model is quite accurate when compared to the experimental data.

The computational results for the simulations are, in both cases, presented in *Figure 3.9*. For all cases with zero degrees of angle of attack, the results are coincident, with the exception of the drag coefficient for the mid-wing. For cases with $4°$ and $8°$ of angle of attack, the results start to diverge in excess. For the high-wing model, the maximum relative error for the lift coefficient is 16.06% and for the drag coefficient it is 17.96%. For the mid-wing model, these errors are, respectively, 12.60% and 20.46%. As stated above and according to Wilcox [14], the $k-\omega$ model tends to overestimate drag, which could explain the difference between the average lift and drag coefficients relative error. Given that in this work the object of study flies at an AOA of $1.07°$, the results of the simulation have a low relative error to the experimental research.

Taking into account the general results, the $k-\omega$ SST model was found to be acceptable and reliable for low AOA scenarios. When compared with experimental curves, computational results follow the same trends as the experimental ones. The model is, therefore, considered validated and ready for use for the remainder of this work.

3.2 Geometry Description

To comply with the objectives of this work and as a way to obtain practical results from it, the aircraft geometry utilised is that of the *UBIAT* team's 2024 entry for the *Air Cargo Challenge* (ACC) competition (*Figure 3.10*), which was kindly provided by the team.

For the purposes of this work, only the fuselage and wing assembly is relevant, with the other components of the aircraft not being taken into consideration for the simulations. Furthermore, due to software and hardware limitations, the original geometry provided by the technical team had to be simplified using *CATIAV5*, removing small protuberances and other structural elements, while preserving the original wireframe composition and ensuring that *Fluent Meshing* is able to accurately model said geometry. Another necessity regarding the geometry is the removal of approximately $1mm$ of the trailing edge of the wing across the whole span. Due to the very small faces occurring in the wing trailing edge, shortening the chord by $1mm$ allows the CAD software to close the surface and create a solid object that can be imported to *Ansys*.

Although these modifications to the original geometry undoubtedly alter the results of the real aircraft, the general shape of the lift and drag curves is minimally changed, as verified in *Section 3.1*. Therefore, the simplified geometry is suitable for use in this analysis.

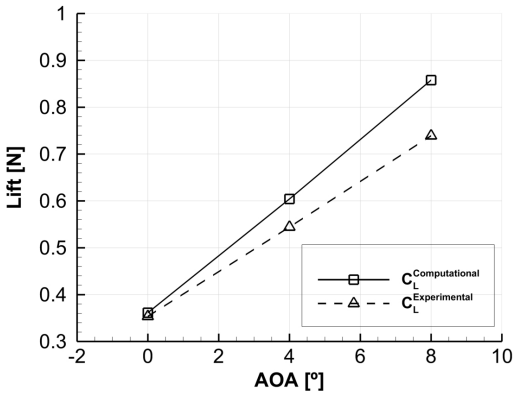

(a) Graphical representation of mid-wing lift coefficient.

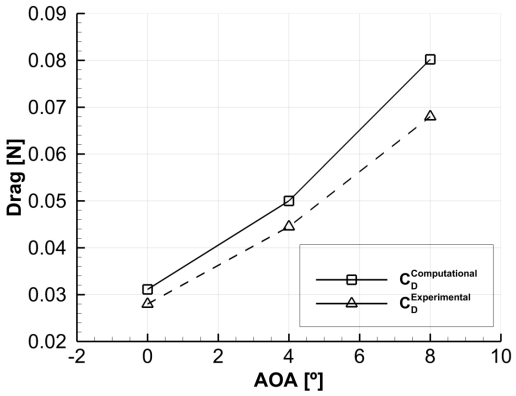

(b) Graphical representation of mid-wing drag coefficient.

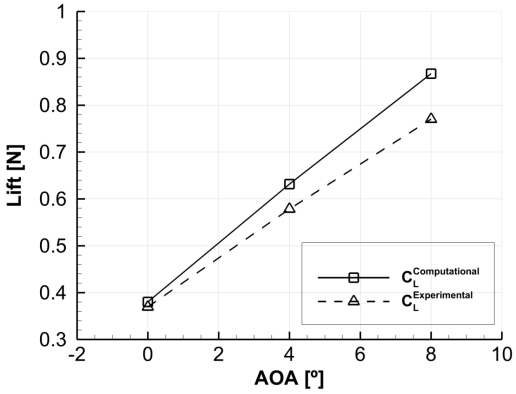

(c) Graphical representation of high-wing lift coefficient.

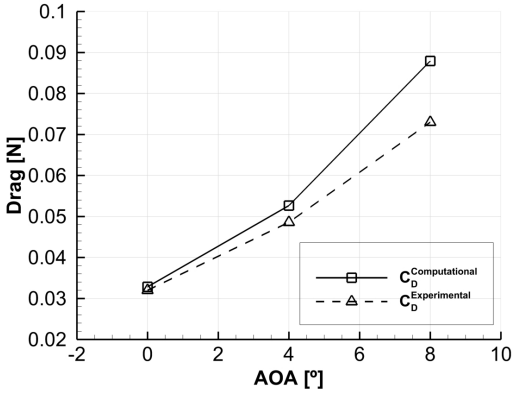

(d) Graphical representation of high-wing drag coefficient.

Figure 3.9: Graphical comparison of computational and experimental results for turbulence model validation.

Figure 3.10: Aircraft designed and built by team UBIAT for ACC2024. Obtained from UBIAT website.

3.2.1 Relevant Variations

Studying the influence of the wing position on the fuselage, and the drag that develops on the interface of both components requires the simulation of several cases that encapsulate the general behaviour of aerodynamic performance across both axes of the fuselage. To

this effect, five positions were modelled and analysed: the original wing position of the wing, two longitudinal positions, and two vertical positions.

Let X be the longitudinal distance from the nose of the aircraft to its tail, normalised by the wing chord ($250mm$), and let Y be the vertical distance from the upper surfacer of the fuselage to the lower surface, normalised by the height of the fuselage ($151.483mm$). For reference, the fuselage is $70.3mm$ high and has an area of $210mm^2$. The original wing position, measured relative to the leading edge, is located at $(X, Y) = (1.555, 0.126)$ and has $1°$ of incidence. The aerofoil used in this small-sized UAV is named *UBIAT2024*, which is a modified version of the S4062 through mean of an optimization algorithm. In *Table 3.3* all five positions analysed in this work for this aircraft are represented, with a corresponding number in the correct position. Two main analysis are performed: an analysis of the horizontal position of the wing (cases $1, 2$ and 3) and an analysis of the vertical position of the wing (cases $2, 4$ and 5).

Table 3.3: Representation of the five wing positions in relation to the fuselage studied in this work.

		X		
Y		0.750	1.555	2.25
	0.126	1	2	3
	0.500		4	
	0.874		5	

All these configurations are achieved through careful translation of the wing along the fuselage using *CATIAV5*, and then through the proper geometric wireframe operations to join all the surfaces and then close them. They are then imported into *Ansys* directly and ready for preparation using *Ansys Discovery*. *Figures 3.11 and 3.12* gather both analysis' models for proper visualisation. With all five cases modelled, it is then necessary to prepare them for *Ansys Fluent*.

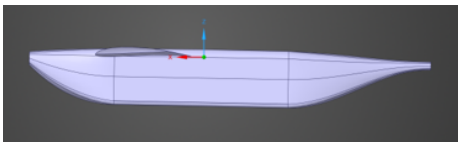

(a) Case 1.

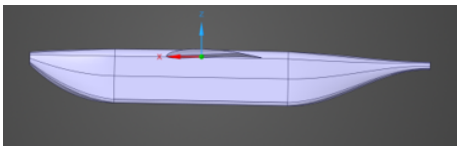

(b) Case 2.

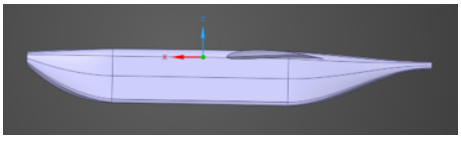

(c) Case 3.

Figure 3.11: Representation of horizontal cases.

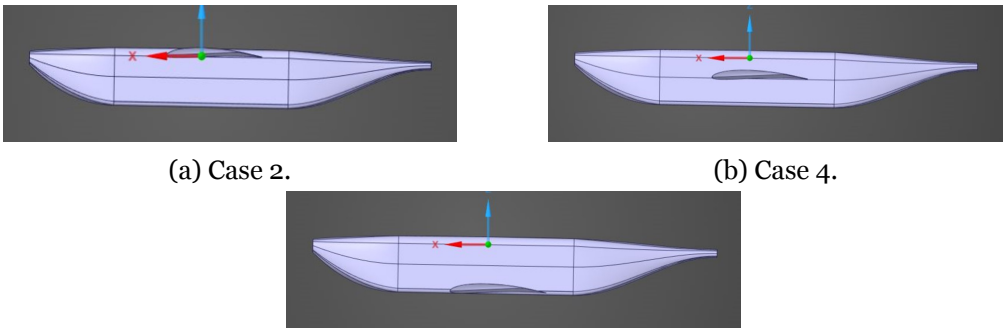

(a) Case 2.

(b) Case 4.

(c) Case 5.

Figure 3.12: Representation of vertical cases.

3.2.2 Circular-section Fuselage

An interesting comparison to make in this work is between the provided square-section fuselage and a circular-section fuselage. In addition to providing insight into how interference drag manifests in different geometries, it also allows for further validation and discussion of the results obtained. For this purpose, the three vertical positions modelled above will be the same presented in this chapter.

The geometrical differences between both fuselages resides in the shape of the two central sections. The square sections were substituted for circular sections of the same height, respecting the total length and shape of the fore and aft sections. The ”Multi-section surface” function of *CATIAV5* was used for the purpose of uniting all four sections, with the use of strategically placed couplings on right-angled points to ensure these are not deformed. Without these couplings, the function would chamfer the corners of the fuselage, which is undesirable. The wing was repurposed from the previous chapter, as no modifications were done to it. *Figure 3.13* represents the three vertical configurations studied for the circular-section fuselage.

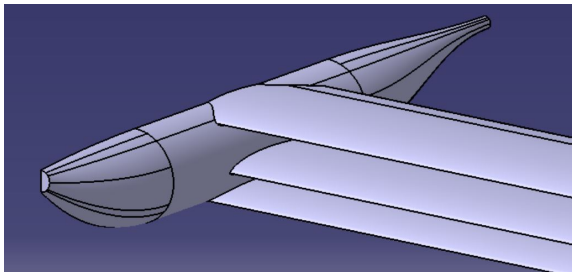

Figure 3.13: Representation of the three configurations for a circular fuselage.

3.3 Geometry and simulation Preparation

The preparation of all configurations was done in the same way as that of the validation cases. This ensures the validity of the results within the boundaries and limitations set for the $k-\omega$ model in *Section 3.1*.

The aircraft's relevant geometrical specifications, alongside the cruise phase flight characteristics are given in *Table 3.4* and are used in the simulation for each case. It should be noted that, as in *Section 3.1*, the geometrical model was cut in half along the longitudinal axis, thereby saving computational and time resources. Thus, the wing area was divided by two to account for this fact. All other parameters remain unchanged.

Table 3.4: Geometrical and cruise flight parameters.

Parameter	Value
Wing Area, $[m^2]$	0.825
Wing Chord, $[m]$	0.250
Cruise AoA, $[^\circ]$	1.07
Cruise Speed, $[m/s]$	22.369

The five simulations with a square-section fuselage were run and converged between 30 and 45 iterations, with the x, y and z scaled residuals not larger than 1×10^{-6}. These are satisfactory results and sufficient for this work to proceed with the aerodynamic analysis.

The high- and mid-wing configurations for the circular-section fuselage converged within the same intervals as the square-section fuselage, with the exception of the low-wing configurations, which demonstrated a repeating pattern from iteration 30 up to iteration 100, where the simulation was manually stopped. An average of 70 iterations was taken as the final result. This is the only case where the turbulence model limitations presented themselves. Interference effects were calculated according to *Section 2.1* , representing the difference between the total configuration drag and the sum of the individual components.

3.4 Fairing Modelling

As per *Section 2.3*, fairings are a useful method to control flow at the interface of the wing and fuselage and to reduce the interference drag of the interface. In this work, two main methods for fairing design are explored, simple chord radii fairings and trailing edge fairings.

Radii fairings are very straightforward to design in *CATIAV5* utilising the "chordal fillet" function. For each vertical position of the wing, both on the upper and lower surface, a chordal fillet of 5% of the wing chord was modelled. This function allows the fillet to be built according the specifications set while also respecting the already existing geometry.

The ”face-face fillet” function was then used to smoothen the trailing edge of the fillet into the fuselage. This guarantees that the fillet is flush and streamlined with the wing and the fuselage.

The value of 5% was set due to geometric constraints in the lower wing surface for the low-wing configuration and in the upper wing surface in the high-wing configuration. *Figure 3.14* provides a visual representation of the three chordal fillets modelled. The simulations for these configurations were performed in accordance with *Section 3.1*. This fairing will be referred to as ”Fairing 1”.

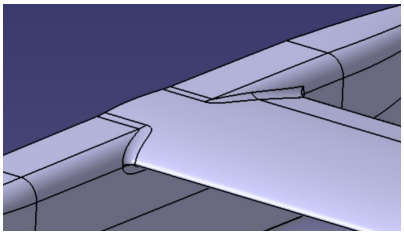

(a) Fairing for configuration 2.

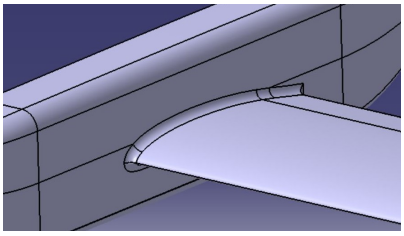

(b) Fairing for configuration 4.

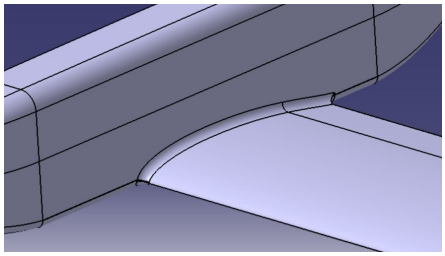

(c) Fairing for configuration 5.

Figure 3.14: Visual representation of the chordal fairings modelled.

Another type of fairing designed for the interface between the fuselage and the wing was modelled according to the work of Maughmer [16] and Klein [15]. These consist of a connection between the aerofoil profile and another profile projected onto the fuselage. This second profile was designed to slightly extend the leading edge of the wing forward and to arch towards an extended curved trailing edge.

Due to geometric and software constraints (*CATIAV5´s Blend* function is unstable), establishing a satisfactory fuselage profile for the fairing proved difficult. A combination of splines, ellipses, and lines was used to best approximate the specifications of Klein [15]. Although extension of the leading edge was also implemented, it was done so to a lesser degree than Maughmer [16] indicated, since, for low angles of attack, the intensity, if any, of the wing root vortices is very low. Extending the leading edge, in these cases, would lead to an increase in induced drag that outweighs the gains in interference drag [6]. The extension of the leading edge was designed to be between $1.5mm$ and $5mm$, with the extension of the trailing edge ending at $62.5mm$ behind the trailing edge of the wing. The wing and fuselage were used as tangent supports for the fairing, ensuring continuity between the surfaces and preventing edges when running simulations. The final result for

the three vertical positions is presented in *Figure 3.15*. With the fuselage profiles clearly visible, it is possible to observe how the upper and lower fuselage limits influence the fairing geometry, considering the middle fairing as optimal. This fairing will be referred to as ”Fairing 2”.

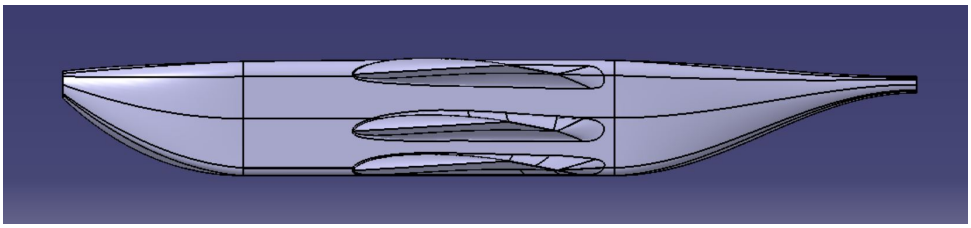

Figure 3.15: Graphical representation of the second fairing model for all vertical positions.

All fairing simulations converged between 40 and 45 and with scaled residuals on the order of magnitude 1×10^{-6}. It must be noted that, for the second fairing model, the number of iterations needed for convergence sat in the higher half of the interval stated above.

Chapter 4

Results and Discussion

4.1 Analysis of Aerodynamic Performance for Several Wing Positions

Having simulated the five presented cases, this chapter focuses on working those data and presenting them along with a detailed analysis of the observed differences. In addition to the drag coefficient and distribution essential for this work, the lift distribution was also calculated to produce a more robust discussion of the results. In terms of mesh and result quality, it must be noted that the values of y^+ were far below one throughout almost all of the model surface, indicating a well-resolved boundary layer. The exceptions to this are the trailing edge of the wing and the posterior flat face of the fuselage, where values for y^+ drastically rose above one.

The results obtained and presented in *Graphs 4.1a and 4.1b* represent the lift and drag coefficients of the horizontal and vertical position of the wing, respectively. Free-flow lift and drag coefficients for the wing and fuselage alone are presented in *Table 4.1* for reference. Interference lift and drag coefficients, lift and drag distributions and skin friction coefficients for all cases are available for consultation in *Appendixes B,C and D respectively*.

Table 4.1: Free flow lift and drag coefficients for the wing and for the fuselage.

	C_L	C_D
Wing	0.473506	0.01853
Fuselage	0.000834	0.003082

It is clear that the forward position of the wing generates the most lift, but also the most drag, with the other two horizontal positions of the wing generating lower aerodynamic forces. It is also noted that the most aft position of the wing generates much lower drag force than the most forward position, which is reflected in the same way in terms of lift. Vertical positioning of the wing also yields interesting results, with the aerodynamic forces much greater in the low-wing position. The near-linearity of the drag curve in both axes is unexpected.

Analysing the interference in lift and drag for the horizontal cases *Table 4.2*, it is clear that, for every case, the interference between the wing and the fuselage is negative, which means that the interference creates a positive effect. This is also stated by Hoerner [6],

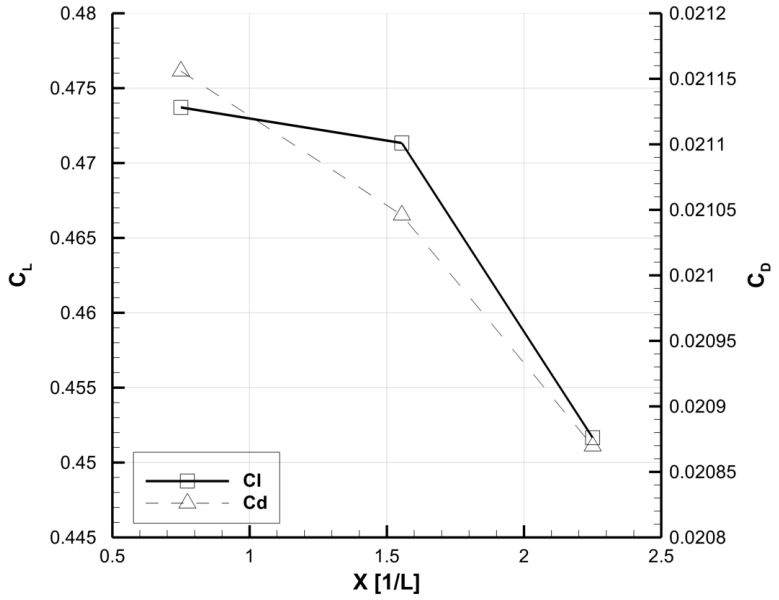

(a) Representation of lift and drag coefficient for three horizontal wing positions.

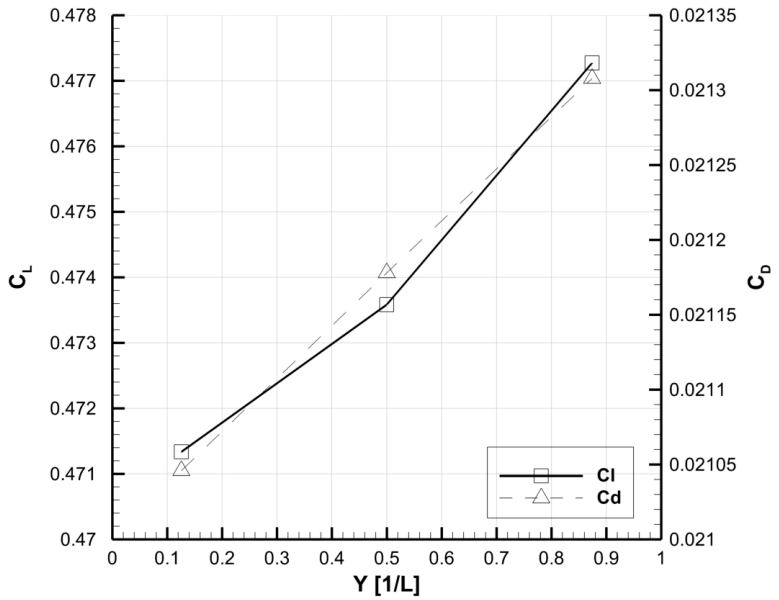

(b) Representation of lift and drag coefficient for three vertical wing positions.

Figure 4.1: Representation of lift and drag coefficients for the analysed wing positions.

who explains that when two surfaces are combined as this, the combined wetted area is reduced, resulting in a total drag value lower than the sum of the free-flow drag values of both components, although interference drag in itself has a positive value.

The experiments presented by Kentfield [20] also corroborate this conclusion but from a main body (fuselage) perspective rather than from a full model drag perspective, such as Hoerner and this work. As stated in a previous chapter, Kentfield studied how short pod-type fuselages influence interference drag on the fuselage and which positions are the most beneficial. The author concluded (for *fuselage Model 1*, which is the most similar to

the aircraft in this work) that the fuselage drag increases considerably with a high-wing forward position and then decreases as the wing moves further aft. For very aft positions, the fuselage drag tends to increase again. Hoerner [6] predicts this phenomenon and explains it as follows.

When a smaller body is placed in the vicinity of another body, the mutual disturbance of their pressure fields modifies drag characteristics. The smaller body experiences drag not only from local dynamic pressure, but also from pressure gradients created by the main body, which alter apparent drag. Hoerner interprets this as a form of "horizontal buoyancy", where the added body is supported or opposed by the pressure differentials of the flow. In addition to this effect on the added body, the altered pressure distribution on the main body also leads to additional pressure drag components. Therefore, the total interference drag consists of two parts: an internal drag, equal and opposite between the two bodies, which cancels out, and a net drag increment that remains due to altered pressure fields. Of course, the magnitude and sign of this net interference drag depend on prevailing pressure gradients: ahead of the main body, negative pressure gradients lead to a maximum drag interference drag, while aft of the main body, positive pressure gradients lead to minimum interference drag. Note how the data are interpreted. Negative interference drag coefficients mean that, although interference is favourable, drag is still generated as a force. In this case, for horizontal position, the module of interference drag increases as the wing moves aft, therefore not contradicting the findings.

To further complete the analysis of the horizontal aerodynamic performance of the wing position, the negative static pressure gradients in the forebody greatly increase the extent of interference caused by an added body in terms of total interference drag, even considering the high interference drag felt by the fuselage. Further along the body, interference drag decreases mainly due to a weaker positive static pressure gradient and subsequent increase in boundary layer thickness. Further aft of the main body, the greater positive static pressure gradient eliminates to a great extent the interference effect caused by the added body.

Table 4.2: Interference drag coefficient for horizontal positions of the wing.

Horizontal Axis			
	X $[1/c]$	C_L	C_D
Position 1	0.750	-0.00063	-0.00046
Position 2	1.555	-0.00300	-0.00057
Position 3	2.25	-0.02268	-0.00074

Analysing the results obtained for the vertical positioning of the wing, low-wing configurations present the highest lift and drag combinations, with these decreasing as the wing moves up. These results are supported by Kentfield [20], who shows that low-wing configurations generate higher drag values than high-wing configurations. Hoerner reaches the same conclusion, the explanation of which is presented below.

α flow is a concept mentioned previously [6] that has significant implications at the interface between the wing and fuselage. To better understand and visualise this concept, a *Python* algorithm [28] was developed that gathers raw data from *Ansys Fluent* and calculates the lift and drag distributions by integrating $-p \times A$ over the span of the aircraft (*Appendix A*). The calculated total drag was then cross-checked with the values outputted by *Fluent* and found to be very accurate. Considering both distributions for the established position four (*Figure 4.3*) in this work and comparing it with a similar case presented by Hoerner (*Figure 4.2*), the similarity is very noticeable. The lift distribution, after being filtered in accordance with *Equation 4.1*, reveals an essentially elliptical distribution, with a distinctly noisy section at $y = 1.00m$, due to geometrical quirks in the aircraft model. Near the interface where the wing meets the fuselage ($y = 0.07m$), lift drops suddenly and then increases again. The peaks mentioned by Hoerner, while not explicit due to the way data is filtered, exist in fact when the trend of raw lift is considered. Hoerner takes this behaviour as an increment in local wing chord, which generates more lift than the wing alone, but also more drag. Furthermore, parasitic losses in the wing root have a corresponding loss in lift, which is also corroborated by Hoerner. Analysing the drag distribution, a distinctive negative drag area is present. The negative drag values observed near the wing–fuselage junction are attributed to local pressure recovery caused by wing–fuselage interference. As described by Hoerner, the fuselage modifies the pressure field at the wing root, producing a favorable pressure gradient that can locally compensate for viscous losses.

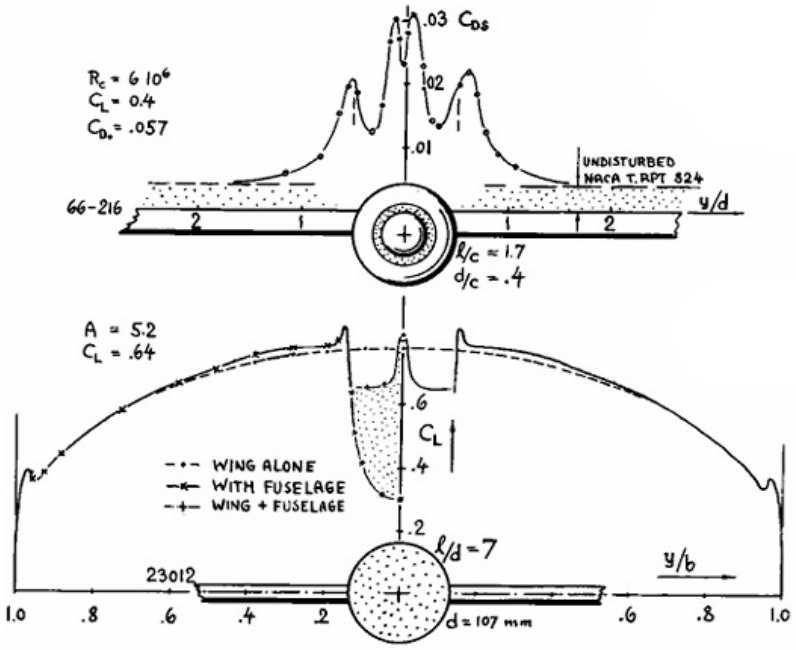

Figure 4.2: Lift and drag distributions as affected by bodies added to the center of wings. Adapted from Hoerner

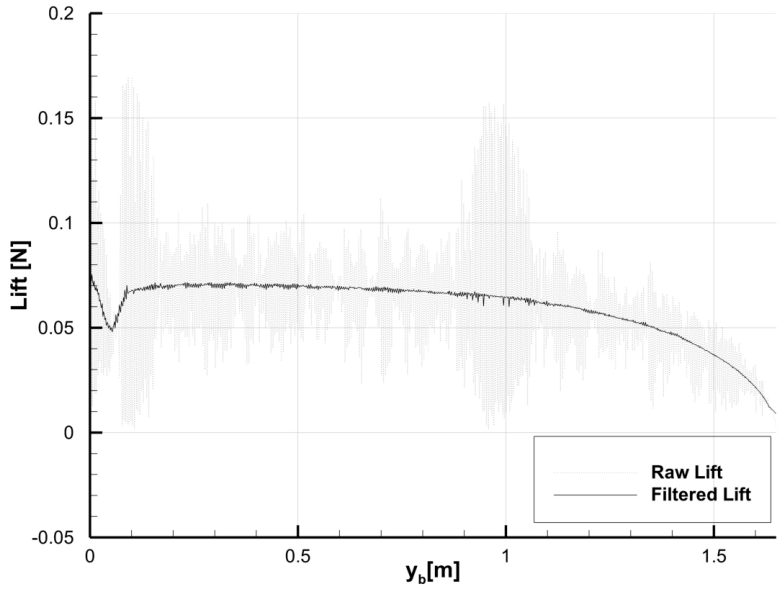

(a) Representation of lift distribution.

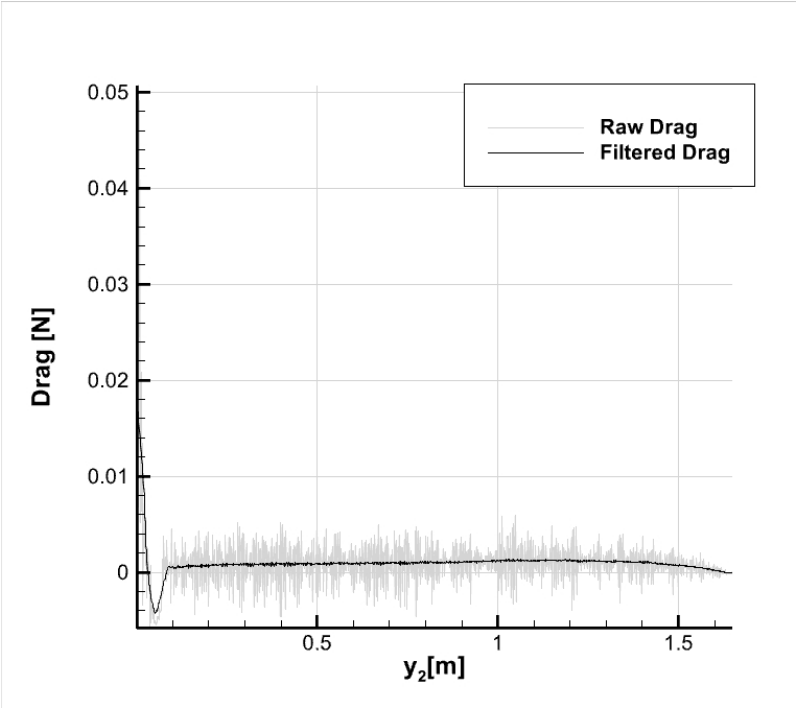

(b) Representation of drag distribution.

Figure 4.3: Representation of lift and drag distributions for position number four.

$$\bar{F}(y_j) = \frac{1}{N} \sum_{i=-k}^{k} F(y_{j+i}), \quad N = 2k + 1 \quad (4.1)$$

The influence of the displacement caused by the main body also leads to stark differences

in the aerodynamic behaviour of the lift and drag curves. The author states that the average flow speed increases over the lower surface of the wing in high-wing configurations (negative C_L increment) and over the upper surface of the wing in low-wing configurations (positive C_L increment), leading, respectively, to a decrease and increase in lift for each configuration. Hoerner further states that for forward high-wing positions, their lift coefficient increment actually becomes positive, and that for very aft positions it becomes more negative. This behaviour then leads to an increase or decrease in the induced drag, depending on the sign of the lift coefficient increment. For high-wing positions, the increase in induced drag is very noticeable, but as the wing moves down the fuselage, the effects due to the vertical position and due to α flow cancel out (*Table 4.3*).

Table 4.3: Interference drag coefficient for vertical positions of the wing.

Vertical Axis			
	X $[1/c]$	C_L	C_D
Position 1	0.750	-0.00300	-0.00057
Position 2	1.555	-0.00076	-0.00043
Position 3	2.25	0.00293	-0.00030

The results are further corroborated by Jacobs' experiments [17], which confirm that low-wing configurations experience higher performance than high-wing configurations in terms of lift and drag figures. However, the author also states that mid-wing positions have a performance comparable to that of high-wing configurations, which is not reflected in the results obtained. This may be explained, in the authors' words, by the way flow develops near the wing-fuselage interface, since stability of the flow, condition of the interface, and geometrical characteristics all contribute to "interference burble". It is stated that moderate-thickness, low-camber aerofoils are more susceptible to this phenomenon, which would fit the description of the geometry used in this work.

Kentfield [20] also produces similar conclusions. Following the previous reasoning concerning the fuselage as the reference measured, the author states that higher drag forces are experienced in low-wing configurations, with a forward, high-wing experiencing the highest drag. Considering these forces as part of the action-reaction pair proposed by Hoerner, the obtained results are in line with what is concluded by Kentfield.

By comparing the results obtained with those achieved by Hoerner's experiments [6], it is possible to corroborate some of the findings in this work. Although the specific geometries are different from each other, the general behaviour of the aerodynamic phenomena is similar enough to derive fruitful conclusions.

Hoerner states that interference drag is smaller near the nose of the aircraft, reaching its maximum aft of the maximum thickness point of the fuselage (considering a streamlined body), and then decreases again towards the end of the fuselage. Hoerner's experiments are gathered from several experimental sets of data, unlike the three different positions presented here, which means that, precision-wise, there are significant differences. How-

ever, the general behaviour of the curves is maintained and respected.

In *Section 2.1.1*, the aerodynamic phenomenon of laminar separation bubbles was touched upon, since they are prevalent in low Reynolds number conditions and in moderately cambered aerofoils. This effect can greatly alter the results for drag and lift values and, as such, is worthy of consideration in this analysis. In his work, Aftar [29] determines and presents a typical friction coefficient curve that exemplifies LSB formation under low Reynolds number and low AOA conditions. *Figure 4.4* presents the skin friction coefficient, C_f, for the upper surface of the wing at $y = 0.125m$ away from the aircraft symmetry plane.

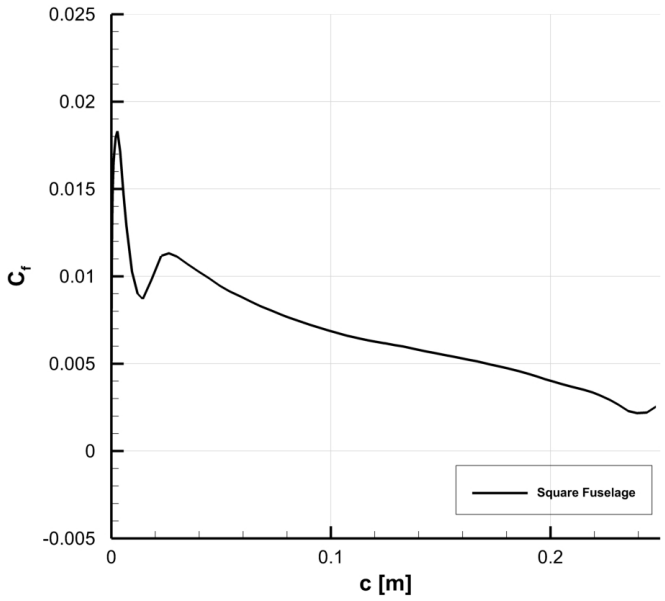

Figure 4.4: Skin friction coefficient for upper wing surface at $y = 0.125m$.

As expected, there is a great increase in C_f as the airflow meets the leading edge that then decreases along the wing chord. At approximately $x/c = 0.18$, C_f increases again, signifying the transition from laminar flow to turbulent flow. Unlike what Aftar presents [29], C_f does not reach zero, and therefore an LSB is not present at this location. These results are consistent across the wingspan of the aircraft for all vertical configurations. Thus, it is safe to conclude that an LSB does not manifest in these results.

4.2 Cross-section Shape Influence in Interference Drag

The shape of the fuselage, as stated by Hoerner [6] and Kentfield [20] is one of the main factors that influences the intensity and effect of interference drag.

The results presented in *Figure 4.6* very well illustrate this effect. The drag coefficient for the circulare fuselage alone was simulated in the same conditions and has the value of $C_D = 0.02869$. Unlike in a square-section fuselage, where drag grows almost linearly as the wing descends in the fuselage, in a circular-section fuselage drag decreases from a

high- to a mid-wing configurations and then greatly increases again for a low-wing configurations. These results are directly in line with those presented by Hoerner [6] and Kentfield [20]. When compared to a curve of parasitic drag for vertical wing position in a circular fuselage (*Figure 4.5*), the curve obtained for interference drag matches extremely well.

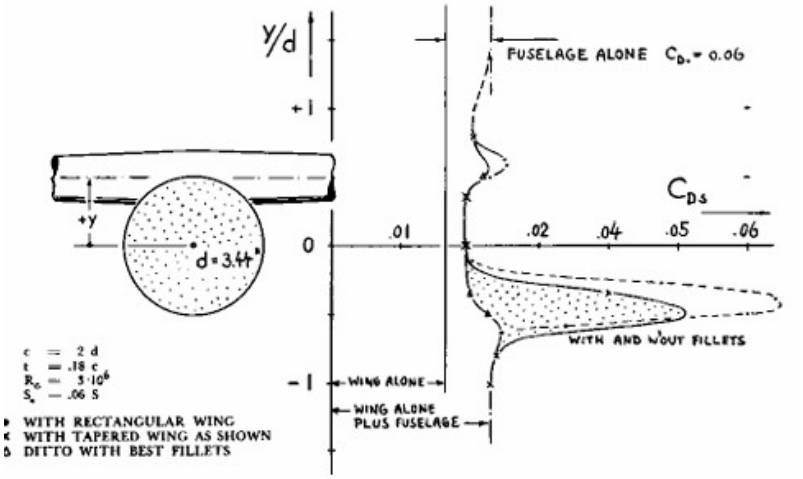

Figure 4.5: Parasite drag coefficient of a wing-fuselage configuration at $C_L = 0.1$. Adapted from Hoerner.

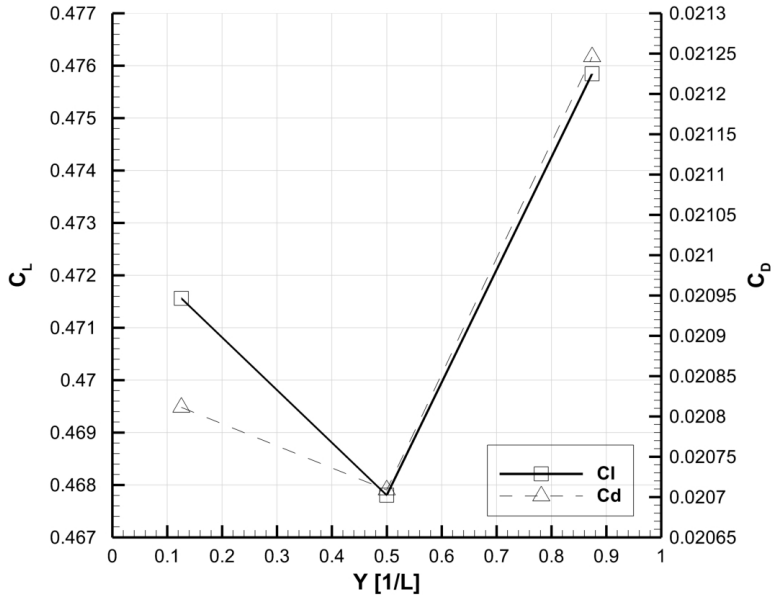

Figure 4.6: Results obtained for the three configurations with circular fuselage.

Looking at interference drag (*Table 4.4*), it is clear it follows the same trend. The interference effect is favourable in every position but more so in a mid-wing configuration. As the wing moves upward or downwards, interference drag increases. These results are, again, in line with Hoerner's work [6].

Table 4.4: Interference drag coefficient for vertical positions with circular-section fuselage.

Vertical Axis			
	Y $[1/L]$	C_L	C_D
Position 2	0.126	-0.00121	-0.00059
Position 4	0.500	-0.00497	-0.00090
Position 5	0.874	0.00307	-0.00037

Comparing directly the drag curves for each fuselage (*Figure 4.7*, the differences become very prevalent. In both cases, the low-wing configurations present the highest total and interference drag, which is already supported by the cited literature. For mid-wing configurations, the circular fuselage presents lower total and interference drag, which contrasts with the higher performance of square-section fuselages for high-wing configurations.

Delving further into the results, it has been stated above that the angle between the wing surface and the fuselage surface can have a significant influence on interference drag. For high-wing configurations, although said angle is largely the same for both fuselage sections, it is considerably acute for the circular-section fuselage, hence increasing drag. For mid-wing configurations, the circular fuselage leads to obtuse angles between the wing and the fuselage, therefore reducing drag. For low-wing configurations, the acute angle between the wing upper surface and the fuselage degrades performance the most. Although this analysis is rather crude, it can provide some insights into the characteristics a particular design might present during the conceptual design phase.

4.3 Influence of Wing Fillets in Aerodynamic Performance

Although the position of the wing on the fuselage is one of the methods to reduce or control interference drag, the introduction of fairings at the interface between the fuselage and the wing is also relevant in this case. *Table 4.5* presents the total lift and drag coefficients for both fairing models.

Table 4.5: Aerodynamic forces for vertical positions of the wing with fairings.

Aerodynamic Coefficients					
		Fairing 1		Fairing 2	
Vertical Axis	Y $[1/L_f]$	C_L	C_D	C_L	C_D
Case 2	0.126	0.477	0.0205	0.472	0.0203
Case 4	0.500	0.478	0.0213	0.476	0.0212
Case 5	0.874	0.478	0.0214	0.478	0.0213

The results of interference drag obtained for the configurations with fillets are presented in *Table 4.6*. When compared with *Table 4.3*, the influence of fillets on interference drag is substantial. For the high-wing configuration, the interference drag more than doubled its favourable effect, with a corresponding decrease of 3.38% in total drag coefficient. For

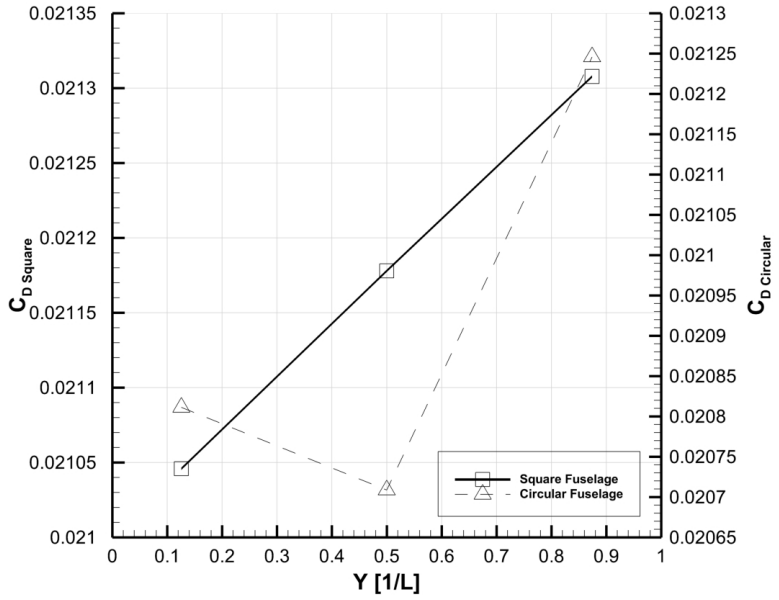

(a) Representation of total drag coefficients for square and circular-section fuselages.

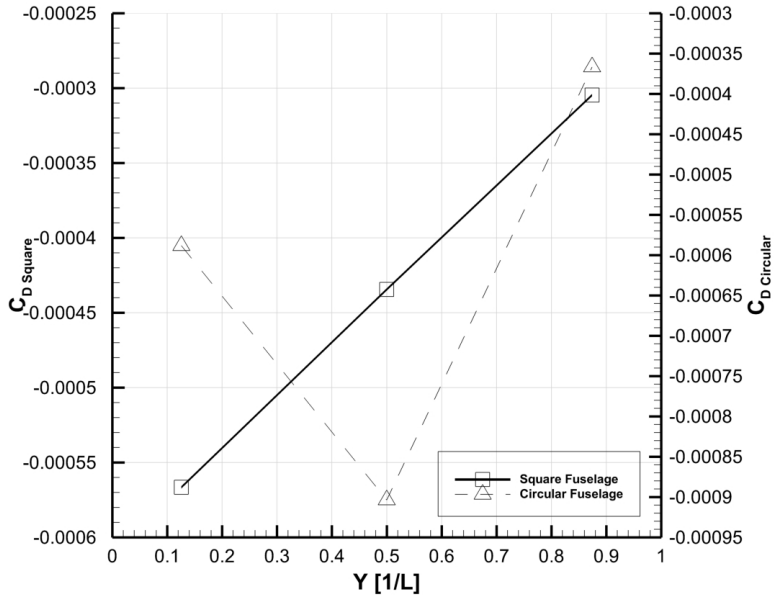

(b) Representation of interference drag coefficients for square and circular-section fuselages.

Figure 4.7: Representation of lift and drag coefficients for the analysed wing positions.

mid and low-wing configurations, when compared to the previous results, interference drag is not significantly altered.

Table 4.6: Interference drag coefficient for vertical positions of the wing with Fairing 1.

Vertical Axis			
	Y $[1/L]$	C_L	C_D
Position 2	0.126	0.00230	-0.00128
Position 4	0.500	0.00883	-0.00039
Position 5	0.874	0.00929	-0.00031

Proceeding with the same analysis for the second fairing model, *Table 4.7* shows the interference coefficients for both drag and lift. The influence of the fairing on drag is positive for all positions, with interference drag being negative every time. Looking at the overall drag coefficients (*Table 4.5*), there is a significant decrease of 2.65% in drag for the high-wing position. For the remaining two, drag is not significantly altered. However, in regards to lift, the presence of the fairing results in a negative increment in lift coefficient for the high-wing position, while, for the other two, the increment in lift coefficient is positive. Still, in all cases, the lift coefficients with the fairing have increased for all positions.

Table 4.7: Interference drag coefficient for vertical positions of the wing with Fairing 2.

Vertical Axis			
	Y $[1/L]$	C_L	C_D
Position 2	0.126	-0.00236	-0.00112
Position 4	0.500	0.00186	-0.00035
Position 5	0.874	0.00405	-0.00026

Hoerner [6] supports these results, explaining that fillets influence mainly interference drag in low and high-wing configurations, where peaks in drag occur. Although this is confirmed for the high-wing configuration, due to the disturbed flow over the wing, for the low-wing configuration, the fairing does not significantly alter drag or lift coefficient values, with these being very similar in the first place. This is mainly due to the geometry of the fuselage and the way the interface is designed. With a square-section fuselage, even with filleted edges or tapered fairings, the flow over the wing in the low-wing configuration studied remains mostly undisturbed, unlike in the high-wing configuration. When compared to the results presented by Klein [15], the results obtained in this work for the low-wing configuration are supported, with the introduction of a fillet influencing aerodynamic performance in a positive manner.

When comparing the increase in aerodynamic performance between both fairing models (*Table 4.8*), it is clear that the introduction of a fairing increases aerodynamic performance. However, the results obtained are not what was expected from Klein's [15] findings. The author states that the fairings can significantly increase performance, as is demonstrated here; however, they also state that the tapered fairings have superior performance, which is not the case with these findings. One possible answer to this disagreement is the geometry of the tapered fairings themselves. In *Chapter 3.4* it is stated that due to geometrical and software limitations, building the fairing geometry proved quite difficult. This may have led to improper surface features, such as small bulges or indentations, which influence the results. The radii distributions may also not be the most favourable for this wing-fuselage interface for the same reasons stated above.

Although the above discussion already provides good insight into how the modelled fairings alter aerodynamic performance, there is still interest in delving further into the drag values obtained. *Ansys Fluent* provides a simple drag breakdown into pressure and vis-

Table 4.8: Increment in aerodynamic efficiency (C_L/C_D) for vertical positions of the wing with fairings.

Aerodynamic L/D increment, [%]					
Vertical Axis	Y $[1/L]$	Fairing 1	L/D	Fairing 2	LD
Case 2	0.126	4.66%	23.43929	2.86%	23.03613
Case 4	0.500	0.62%	22.5011	0.15%	22.39552
Case 5	0.874	0.19%	22.44224	0.03%	22.46612

cous drag, which can be exported and compared. *Table 4.9* presents the viscous and pressure drag components for the vertical positions and the two fairing variations. The data suggests that fairings are especially beneficial in terms of reducing viscous drag, which is expected, but tend to increase pressure drag due to the increase in frontal surface area of the aircraft. As discussed before, the fairings appear only favourable for the high-wing configuration, with the other two positions presenting no significant alterations in viscous drag. In terms of pressure drag, all fairings led to an increase in drag, with the exception of the constant radius fairing. Once again, the aerodynamic gains of the first fairing type are confirmed.

Table 4.9: Results obtained for pressure and viscous drag components for all vertical positions and fairing variations.

		Drag Components							
		No fairing			Fairing 1			Fairing 2	
Vertical Axis	Y $[1/L_f]$	Pressure	Viscous		Pressure	Viscous		Pressure	Viscous
Case 2	0.126	0.008008	0.013066		0.08%	-5.43%		1.20%	-4.94%
Case 4	0.500	0.008103	0.013221		0.82%	-0.10%		0.87%	0.12%
Case 5	0.874	0.008076	0.013176		-0.01%	-0.01%		0.27%	0.17%

With these remarks, the benefit of introducing fairings to the junction between the wing and the fuselage is clear. In the simplest of cases, considering a chordal fillet with 5% radius, the aerodynamic performance increased by 4.66% for high-wing configurations, with marginal increases for mid- and low-wing configurations. These same results are also applicable to tapered trailing edge fairings to a lesser extent.

Chapter 5

Conclusions and Recommendations

5.1 Summary

Interference drag is present in every aircraft whenever two independent components are externally joined. When it comes to parasitic drag, the interface between the fuselage and the wing is one of the main contributors, resulting in a loss of efficiency and possibly undesirable aerodynamic phenomena. Although other drag components are associated with the interface, such as induced drag, viscous separations, and profile drag, interference drag was the focus of this work.

This work delved into how the position of the wing on the fuselage impacts interference drag and how it can be mitigated through the employment of fairings. Utilising as a base the 2024 Air Cargo Challenge entry by Team UBIAT, it was possible to analyse how aerodynamic efficiency would be affected by the position of the wing and two different types of fairings.

To validate the results obtained from *Ansys Fluent* CFD simulations, a thorough validation process was followed and documented in detail. A brief analysis of commonly used turbulence models was done, from which the $k-\omega$ SST model emerged as the most suitable for the purposes of this work. The work of Parkin [23] was selected as the basis for this validation and, as such, all necessary geometries were modelled accordingly. A mesh study was done to ascertain the mesh size necessary to guarantee mesh independence, with a smallest element size of $0.0001mm$ considered adequate. The parameters and simulation data were set according to the recommendation and geometric data and the simulations were run until convergence, with a satisfactory value of 1×10^{-6} for the scaled residuals. With a maximum relative error of 10%, the model was considered validated with some considerations.

The main topic of this dissertation was then tackled, beginning with the preparation of the geometry. The CAD model kindly provided by Team UBIAT was prepared to represent the five positions determined relevant for this work and was then imported into *Fluent* for meshing and simulation. The simulations were performed according to the validation methodology, with satisfactory convergence results.

The results proved to be rather interesting, with several possible phenomena present in any given configuration. For all five combinations studied, the interference drag appears as a favourable force, which is unexpected. In terms of horizontal positioning of the wing,

it is shown that a forward wing position, while generating the highest total drag of the horizontal configurations, is the one with the lowest interference drag, due to the effect of negative pressure gradients on the airflow over the surface of the model. As the wing moves aft, the total drag decreases, but the effect of pressure gradients over the length of the fuselage leads to an increase in interference drag. In regards to the vertical positioning of the wing, the low-wing configuration is, unexpectedly, that which produces the higher total lift and drag values but the lowest interference drag. As the wing moves upward on the fuselage, both total lift and drag decrease, with a complementary increase in interference drag.

These results are the culmination of a series of aerodynamic processes that occur at the same time. On the one hand, the pressure gradients and flow over the fuselage lead to a decrease in total drag as the wing moves forward, with the overarching argument that high-wing configurations have negative lift increments, which influences total drag. On the other hand, the fact that the fuselage has a square section leads to a performance that is rather higher than expected from the bibliography. Since the wing joins the fuselage at or over an angle of $90°$, the effects of interference are rather reduced, since airflow over the upper surface of the wing is mostly undisturbed, apart from the high-wing configuration, which takes the brunt of the flow from the nose of the aircraft.

When compared to a circular-section fuselage, low-wing configurations present the highest total and interference drag due to modifications of airflow over the upper surface of the wing, which have the most influence on aerodynamic performance. For mid-wing configurations, the shape of the circular-section fuselage yielded a lower total and interference drag than the square-section fuselage, due to the airflow over the wing root not being as disturbed. In low-wing configurations the shape of the circular-section fuselage largely influence the upper surface of the wing, increasing total and interference drag, unlike in the square-section fuselage. Overall, the results conform to the literature.

The introduction of fairings has also proved to be very beneficial for high-wing configurations. Two types of fairing were modelled according to the bibliography: a constant-radius chordal fillet and a blended curved tapered trailing edge surface. Against expectations derived from said bibliography, the constant radius fairing delivered far more satisfactory results, with a increase in aerodynamic efficiency of 4.7%. The more complex fairing still yielded positive results, though the gains in efficiency were just 2.9% in total. For mid- and low-wing configurations, the use of fairings can be considered negligible, which was expected.

The simulations undertaken in this dissertation, while clarifying on the surface, lack a more detailed analysis of a parametric setup and finer simulation parameters, such as mesh size and turbulent model constants. Thus, further work would be required to reach a definitive profile for the lift and drag curves in different aircraft configurations.

5.2 Concluding Remarks

This dissertation concludes that, for the case-study undertaken, a mid-wing configuration presents the lowest interference drag coefficient and a high-wing presents the highest. Furthermore, a forward high-wing presents the highest total drag and lowest interference drag.

Comparing the results of the square-section fuselage to a circular-section fuselage demonstrated that high-wing configurations are the most favourable while for a circular-section fuselage a mid-wing configurations yields the best results in terms of drag.

The use of fairings has proven beneficial only for a high-wing configuration, granting a 4.66% increase in aerodynamic efficiency in the case of constant radius fairings. Extended tapered fairings provided worse results.

5.3 Future Work

Future work that could be further explored in regards to the topic of the aerodynamic influence of the position of the wing on the fuselage spans every chapter discussed above:

- A drag decomposition algorithm based on free stream and wake measurements could be developed in order to better assess the proportions of induced and profile drag for each configuration, and to further decompose profile drag into its own components;
- Other fairing types would be beneficial for analysis, providing further data for comparison; furthermore, a standardised method for fairing modelling would greatly reduce heterogeneity in the structures and the results;
- An off-design analysis is essential for ascertaining if a particular configuration and fairing type is efficient and performs as desired in other operating conditions, such as take-off or landing; this would also have a synergy with the first point above;
- Utilising a turbulence model better capable of capturing and exacting turbulent phenomena would greatly improve the precision of the results; reducing the mesh size further would increase this precision even more, given drag could converge further with the reduction of mesh size.

References

[1] K. Telli, O. Kraa, Y. Himeur, A. Ouamane, M. Boumehraz, S. Atalla, and W. Mansoor, "A comprehensive review of recent research trends on unmanned aerial vehicles (uavs)," *Systems*, vol. 11, no. 8, 2023. [Online]. Available: https://www.mdpi.com/2079-8954/11/8/400 1

[2] S. Gudmundsson, *General Aviation Aircraft Design: Applied Methods and Procedures*, 2nd ed. Oxford, UK: Butterworth-Heinemann, 2021, expanded content including design guidance for seaplanes, biplanes, UAS, high-speed business jets, and electric airplanes. [Online]. Available: https://books.google.com/books/about/General_Aviation_Aircraft_Design.html?id=VXcrEAAAQBAJ 1

[3] D. P. Raymer, *Aircraft Design: A Conceptual Approach*, 6th ed., ser. AIAA Education Series. Reston, Virginia: American Institute of Aeronautics and Astronautics (AIAA), 2018, covers fundamental principles and practical applications of aircraft design, widely used in academia and industry. [Online]. Available: https://arc.aiaa.org/doi/book/10.2514/4.105361 1, 6, 7, 8

[4] J. John D. Anderson, *Fundamentals of Aerodynamics*, 3rd ed., ser. McGraw-Hill Series in Aeronautical and Aerospace Engineering. Boston: McGraw-Hill, 2001, includes bibliographical references and index. 5, 6

[5] C. P. van Dam, "Recent experience with different methods of drag prediction," *Progress in Aerospace Sciences*, vol. 35, no. 8, pp. 751–798, 1999. [Online]. Available: https://doi.org/10.1016/S0376-0421(99)00009-3 7, 20, 21

[6] S. F. Hoerner, *Fluid-Dynamic Drag: Practical Information on Aerodynamic Drag and Hydrodynamic Resistance*. Brick Town, NJ: Hoerner Fluid Dynamics, 1965, self-published. [Online]. Available: https://archive.org/details/FluidDynamicDragHoerner 7, 10, 15, 37, 39, 41, 42, 44, 45, 46, 49

[7] J. Winslow, H. Otsuka, B. Govindarajan, and I. Chopra, "Basic understanding of airfoil characteristics at low reynolds numbers ($10^4 - 10^5$)," *Journal of Aircraft*, vol. 55, no. 3, pp. 1050–1061, 2018. [Online]. Available: https://doi.org/10.2514/1.C034415 8, 9

[8] A. K. Gupta, P. A. A. Narayana, and G. Ramesh, "Effect of turbulence intensity on low reynolds number airfoil aerodynamics," *International Journal of Engineering & Technology*, vol. 7, no. 4.25, 2018. [Online]. Available: https://doi.org/10.14419/ijet.v7i4.25.22240 9

[9] M. Méheut and D. Bailly, "Drag-breakdown methods from wake measurements," *AIAA Journal*, vol. 46, no. 4, pp. 847–862, April 2008, accessed: 2025-02-09. [Online]. Available: https://doi.org/10.2514/1.29051 10, 12

[10] C. M. E. “Progress towards a method for the measurement of the components of the drag of a wing of finite span,” Royal Aircraft Establishment, Farnborough, UK, Technical Report RAE TR 72232, 1972. [Online]. Available: https://resolver.tudelft.nl/uuid:bf983229-c502-4d9e-a3c7-f31e31821bf2 11, 12

[11] D. C. Wilcox, “Reassessment of the scale-determining equation for advanced turbulence models,” *AIAA Journal*, vol. 26, no. 11, pp. 1299–1310, 1988. [Online]. Available: https://doi.org/10.2514/3.10041 12

[12] ——, *Turbulence Modeling for CFD*, 3rd ed. La Cañada, California: DCW Industries, 2006. [Online]. Available: https://www.amazon.com/Turbulence-Modeling-Third-David-Wilcox/dp/1928729088 13

[13] F. R. Menter, “Improved two-equation k-omega turbulence models for aerodynamic flows,” NASA Ames Research Center, Moffett Field, CA, Tech. Rep. NASA-TM-103975, October 1992, nASA Technical Memorandum 103975. [Online]. Available: https://ntrs.nasa.gov/citations/19930013620 13

[14] D. C. Wilcox, “Turbulence modeling: An overview,” in *39th Aerospace Sciences Meeting and Exhibit*, American Institute of Aeronautics and Astronautics (AIAA). Reno, NV: AIAA, January 2001, aIAA Paper 2001-0724. [Online]. Available: https://arc.aiaa.org/doi/10.2514/6.2001-0724 13, 32

[15] A. L. Klein, “Effect of fillets on wing-fuselage interference,” *Transactions of the American Society of Mechanical Engineers*, vol. 56, no. 1, pp. 1–7, 02 1934. [Online]. Available: https://doi.org/10.1115/1.4019639 14, 37, 49

[16] M. Maughmer, D. Hallman, R. Ruszkowski, G. Chappel, and I. Waitz, “Experimental investigation of wing/fuselage integration geometries,” *Journal of Aircraft*, vol. 26, no. 8, pp. 705–711, August 1989. [Online]. Available: https://arc.aiaa.org/doi/10.2514/3.45828 14, 17, 37

[17] E. N. Jacobs and K. E. Ward, “Interference of wing and fuselage from tests of 209 combinations in the NACA variable-density tunnel,” National Advisory Committee for Aeronautics, Langley Memorial Aeronautical Laboratory, Hampton, VA, Tech. Rep. Technical Report No. 540, 1936, accessed via NASA Technical Reports Server (NTRS). [Online]. Available: https://ntrs.nasa.gov/api/citations/19930091613/downloads/19930091613_Update.pdf 14, 44

[18] L. R. Kubendran, H. McMahon, and J. Hubbartt, “Interference drag in a simulated wing-fuselage juncture,” NASA, Langley Research Center, NASA Contractor Report NASA CR-3811, July 1984, available at https://ntrs.nasa.gov/api/citations/19840021784/downloads/19840021784.pdf. 16, 17

[19] L. Bernstein and S. Hamid, “On the effect of a strake-like junction fillet on the lift and drag of a wing,” *The Aeronautical Journal*, vol. 100, no. 992, pp. 39–52, 1996. [Online]. Available: https://doi.org/10.1017/S0001924000027275 16

[20] J. Kentfield and H. Jones, “Fuselage-wing interference drag of aircraft with relatively short, pod-type, fuselages,” in *40th AIAA Aerospace Sciences Meeting & Exhibit*, Reno, NV, U.S.A., January 2002. [Online]. Available: https://arc.aiaa.org/doi/10.2514/6.2002-708 17, 40, 41, 44, 45, 46

[21] W. Song and P. Lv, “Two-level wing-body-fairing optimization of a civil transport aircraft,” *Journal of Aircraft*, vol. 48, no. 6, pp. 2114–2121, 2011. [Online]. Available: https://doi.org/10.2514/1.C031472 18

[22] N. M. B. Matos and A. C. Marta, “Aerodynamic shape optimization of wing–fuselage intersection for minimum interference drag,” *Aerospace*, vol. 12, no. 5, p. 369, 2025. [Online]. Available: https://doi.org/10.3390/aerospace12050369 19

[23] J. H. Parkin and G. J. Klein, “The interference between the body and wings of aircraft,” *The Journal of the Royal Aeronautical Society*, vol. 34, no. 229, p. 1–91, 1930. 24, 31, 32, 51

[24] A. Tools, “Usa-27 airfoil,” http://airfoiltools.com/airfoil/details?airfoil=usa27-il, 1919, accessed: 2025-05-30. 25

[25] André Deperrois, “XFLR5: analysis tool for airfoils, wings, and planes,” 2023, accessed: 2025-10-03. [Online]. Available: https://www.xflr5.tech/ 25

[26] ANSYS, Inc., “ANSYS discovery: simulation-driven 3d design software,” 2024, accessed: 2025-10-03. [Online]. Available: https://www.ansys.com/products/3d-design/ansys-discovery 27

[27] Environment and Climate Change Canada, “Monthly climate data for toronto, ontario (1927),” https://climate.weather.gc.ca/climate_data/monthly_data_e.html?StationID=5051&timeframe=3&StartYear=1927&EndYear=1927, 1927, accessed on 2025-06-04. Historical data provided by Environment and Climate Change Canada. Data covers monthly summaries for the Toronto climate station (Station ID: 5051). [Online]. Available: https://climate.weather.gc.ca/climate_data/monthly_data_e.html?StationID=5051&timeframe=3&StartYear=1927&EndYear=1927 28

[28] Python Software Foundation, *Python Documentation*, version 3.13 ed., Python Software Foundation, Beaverton, OR, USA, 2025, online; accessed 30 September 2025. [Online]. Available: https://docs.python.org/3/ 42

[29] S. M. A. Aftab, A. S. Mohd Rafie, N. A. Razak, and K. A. Ahmad, “Turbulence model selection for low reynolds number flows,” *PLoS ONE*, vol. 11, no. 4, p. e0153755, 2016, published April 22, 2016. [Online]. Available: https://journals.plos.org/plosone/article?id=10.1371/journal.pone.0153755 45

Appendix A

Python algorithm for lift and drag distribution calculation.

In *Appendix A* the *Python* algorithm used to process the raw surface data extracted from *Ansys Fluent* is presented. Data is extracted from the source *Excel* file containing the following *Ansys* variables:

- ”y”;
- ”pressure”;
- ”face-area-magnitude”;
- ”x-face-area”;
- ”x-wall-shear”;
- ”y-face-area”;
- ”y-wall-shear”;
- ”z-face-area”;
- ”z-wall-shear”.

Lift and drag is then calculated for every cell and integrated across the whole span of the aircraft. Due to noise in the data, a simple rolling average algorithm is implemented to soften the curves.

```
import pandas as pd
import matplotlib.pyplot as plt

# ------------------------------
# 1 Load CSV
# ------------------------------
df = pd.read_csv("POS2_ORG.csv")  # update with your file name

# ------------------------------
# 2 Compute face forces
# ------------------------------
# Pressure contributions (using area vector components)
df["Fx_pressure"] = df["pressure"] * df["x-face-area"]
```

```
14 df["Fy_pressure"] = df["pressure"] * df["y-face-area"]
15 df["Fz_pressure"] = df["pressure"] * df["z-face-area"]
16
17 # Shear contributions (if available; use scalar face area!)
18 if {"x-wall-shear", "y-wall-shear", "z-wall-shear", "face-area-magnitude"}.
       issubset(df.columns):
19     df["Fx_shear"] = df["x-wall-shear"] * df["face-area-magnitude"] * df["x-
           face-area"]
20     df["Fy_shear"] = df["y-wall-shear"] * df["face-area-magnitude"] * df["y-
           face-area"]
21     df["Fz_shear"] = df["z-wall-shear"] * df["face-area-magnitude"] * df["y-
           face-area"]
22 else:
23     df["Fx_shear"] = 0.0
24     df["Fy_shear"] = 0.0
25     df["Fz_shear"] = 0.0
26
27 # Total forces per face
28 df["Fx_face"] = df["Fx_pressure"] + df["Fx_shear"]
29 df["Fy_face"] = df["Fy_pressure"] + df["Fy_shear"]
30 df["Fz_face"] = df["Fz_pressure"] + df["Fz_shear"]
31
32 # ----------------------------
33 # 3 Define spanwise coordinate
34 # ----------------------------
35 df["yb"] = df["y"]  # spanwise position (adjust if needed)
36
37 # ----------------------------
38 # 4 Bin spanwise data
39 # ----------------------------
40 n_bins = 1000
41 yb_min = df["yb"].min()
42 yb_max = df["yb"].max()
43 bins = pd.interval_range(start=yb_min, end=yb_max, periods=n_bins)
44 df["bin"] = pd.cut(df["yb"], bins=bins)
45
46 # Forces per bin
47 lift_per_bin = df.groupby("bin")["Fz_face"].sum()
48 drag_per_bin = df.groupby("bin")["Fx_face"].sum()
49
50 # Bin midpoints for plotting
51 yb_mid = [interval.mid for interval in lift_per_bin.index]
52
53 # ----------------------------
54 # 5 Apply moving average filter
55 # ----------------------------
56 window_size = 21
```

```
57 lift_filtered = lift_per_bin.rolling(window=window_size, center=True,
       min_periods=1).mean()
58 drag_filtered = drag_per_bin.rolling(window=window_size, center=True,
       min_periods=1).mean()
59
60 # ----------------------------
61 # 6 Plot results
62 # ----------------------------
63 plt.figure(figsize=(10,6))
64 plt.plot(yb_mid, lift_per_bin, label="Raw Lift")
65 plt.plot(yb_mid, lift_filtered, label="Filtered Lift", linewidth=2)
66 plt.xlabel("Spanwise Position y (m)")
67 plt.ylabel("Lift per Strip (N)")
68 plt.title("Spanwise Lift Distribution")
69 plt.legend()
70 plt.grid(True)
71 plt.show()
72
73 plt.figure(figsize=(10,6))
74 plt.plot(yb_mid, drag_per_bin, label="Raw Drag")
75 plt.plot(yb_mid, drag_filtered, label="Filtered Drag", linewidth=2)
76 plt.xlabel("Spanwise Position y (m)")
77 plt.ylabel("Drag per Strip (N)")
78 plt.title("Spanwise Drag Distribution (Pressure + Shear)")
79 plt.legend()
80 plt.grid(True)
81 plt.show()
82
83 # ----------------------------
84 # 7 Compute totals
85 # ----------------------------
86 total_lift_raw = lift_per_bin.sum()
87 total_lift_filtered = lift_filtered.sum()
88 total_drag_raw = drag_per_bin.sum()
89 total_drag_filtered = drag_filtered.sum()
90
91 print(f"Total Lift (Raw): {total_lift_raw:.2f} N")
92 print(f"Total Lift (Filtered): {total_lift_filtered:.2f} N")
93 print(f"Total Drag (Raw): {total_drag_raw:.2f} N")
94 print(f"Total Drag (Filtered): {total_drag_filtered:.2f} N")
95
96 # ----------------------------
97 # 8 Save results
98 # ----------------------------
99 output_df = pd.DataFrame({
100     "yb": yb_mid,
101     "Lift_Raw": lift_per_bin.values,
```

```
102     "Lift_Filtered": lift_filtered.values,
103     "Drag_Raw": drag_per_bin.values,
104     "Drag_Filtered": drag_filtered.values
105 })
106 output_df.to_csv("spanwise_forces_filtered.csv", index=False)
```

Listing A.1: Python algorithm developed for calculations of lift and drag distribution based on model surface parameters.

,

Appendix B

Interference Drag and Lift Graphs for various configurations

In *Appendix B* the interference drag and lift coefficients for all cases are graphically represented for consultation.

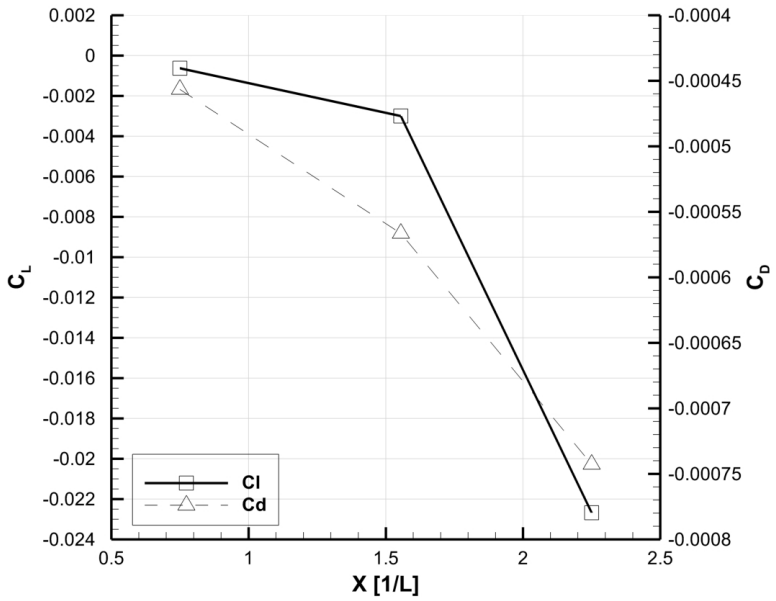

Figure B.1: Representation of lift and drag interference coefficients for horizontal configurations.

,

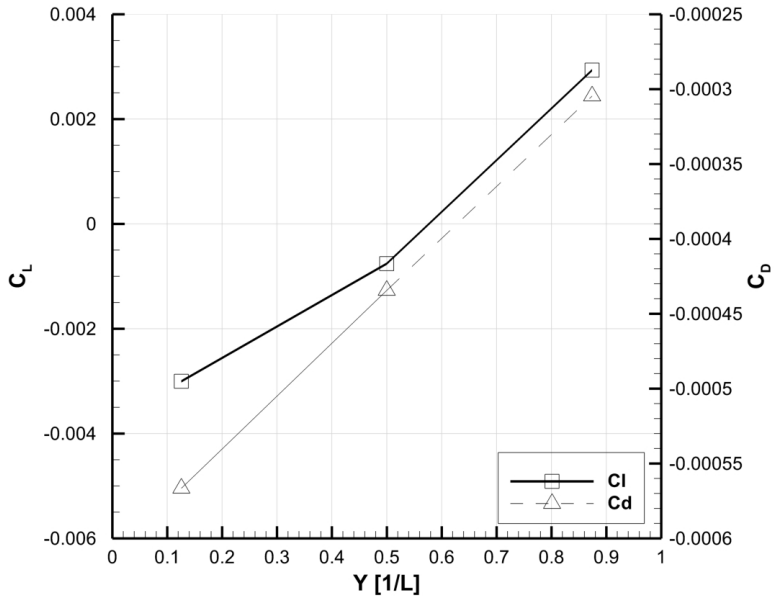

Figure B.2: Representation of lift and drag interference coefficients for Vertical configurations.

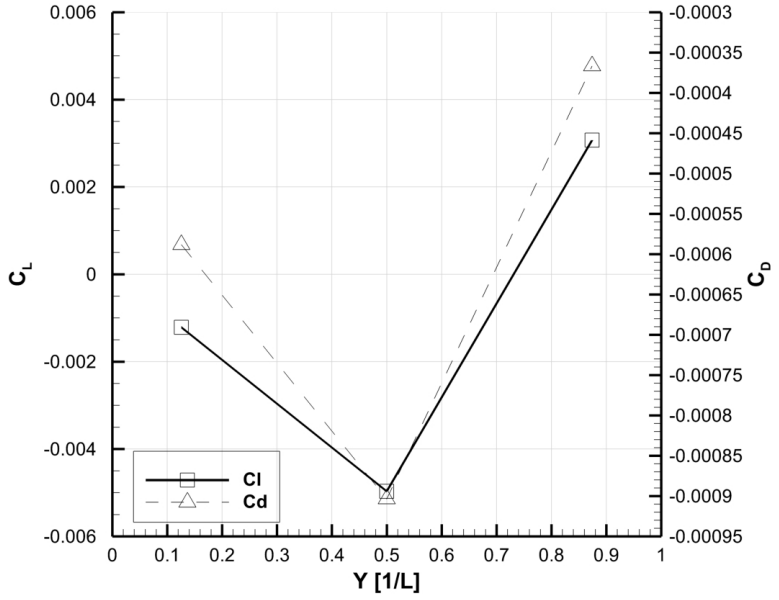

Figure B.3: Representation of lift and drag interference coefficients for circular-section fuselage configurations.

Appendix C

Lift and drag distributions for various configurations

In *Appendix C* the lift and drag distributions for all cases are graphically represented for consultation.

,

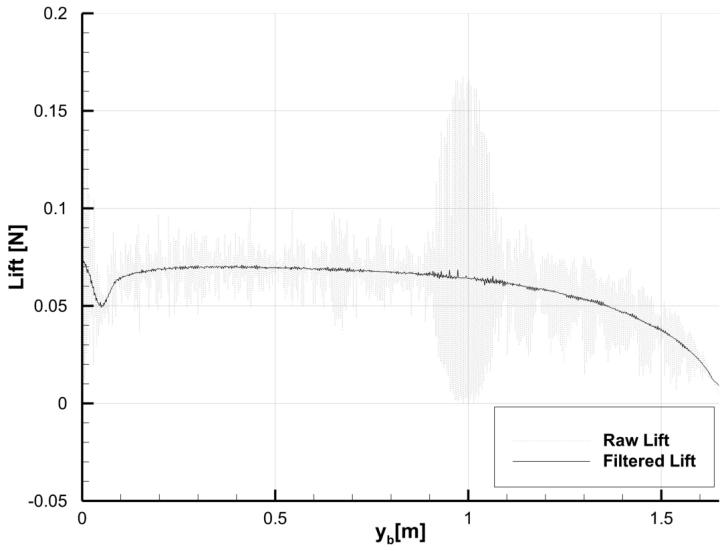

(a) Representation of lift distribution.

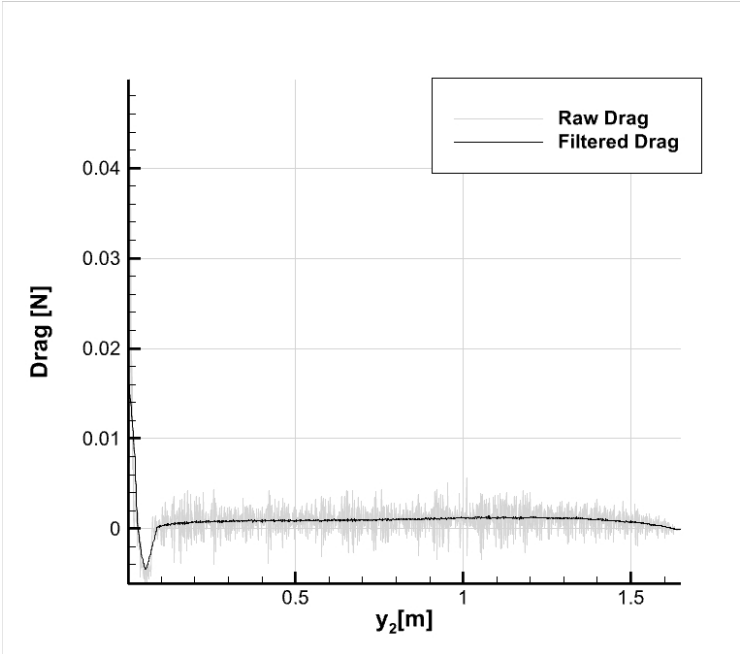

(b) Representation of drag distribution.

Figure C.1: Representation of lift and drag distributions for position number two.

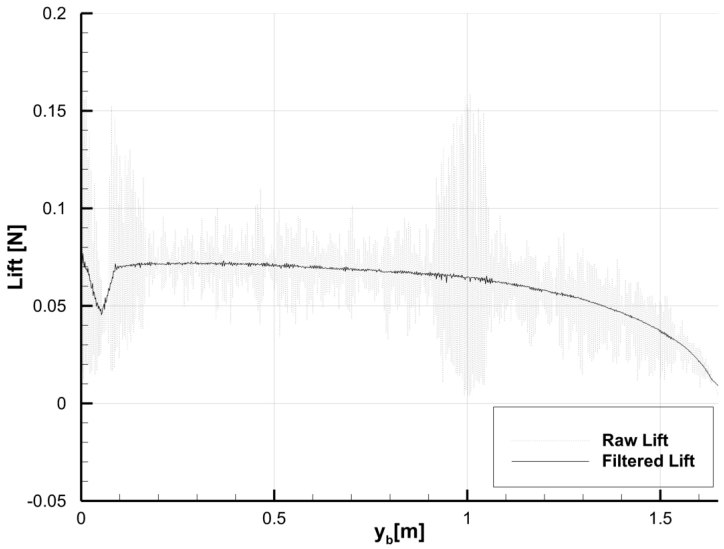

(a) Representation of lift distribution.

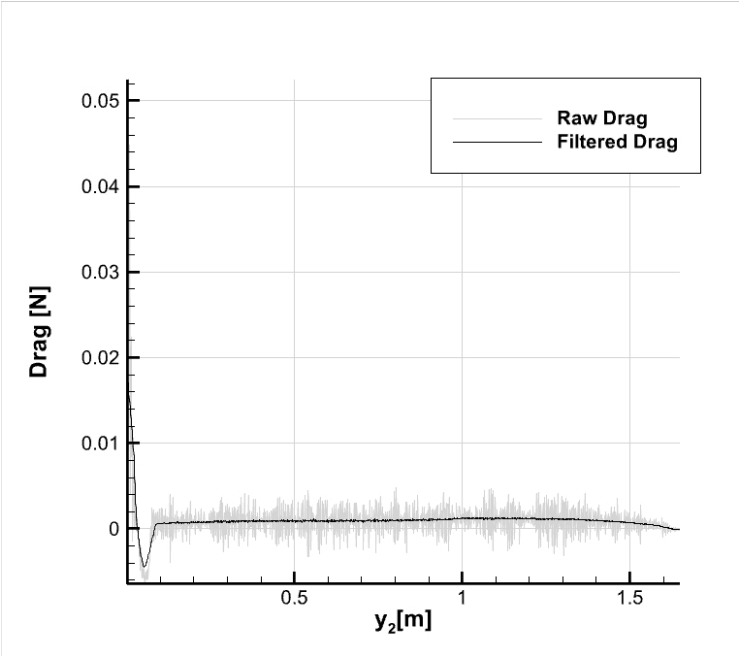

(b) Representation of drag distribution.

Figure C.2: Representation of lift and drag distributions for position number five.

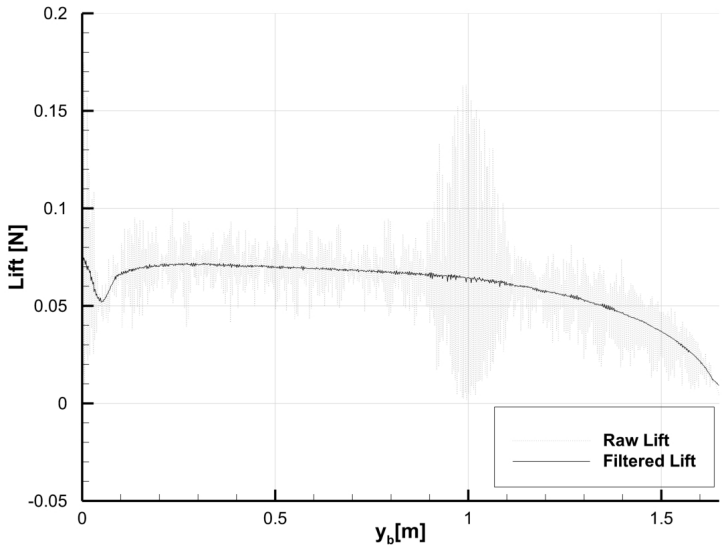

(a) Representation of lift distribution.

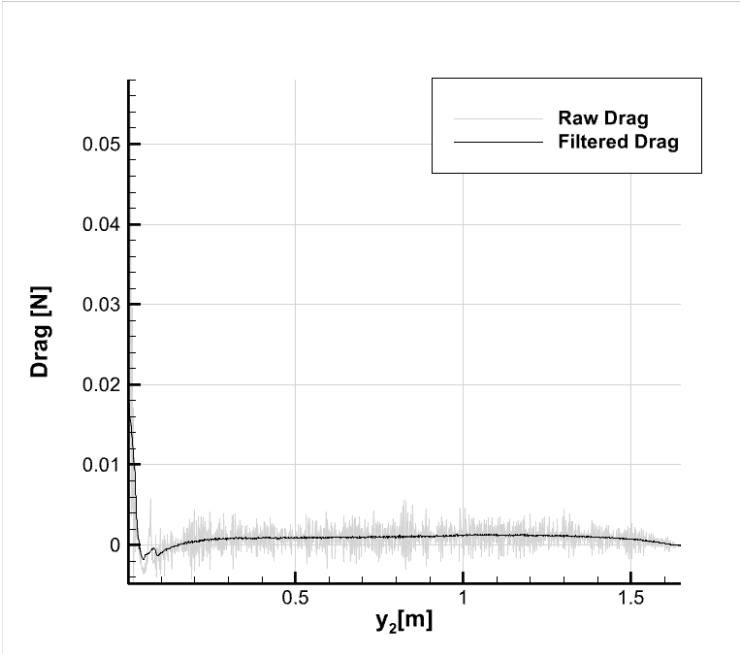

(b) Representation of drag distribution.

Figure C.3: Representation of lift and drag distributions for position number one.

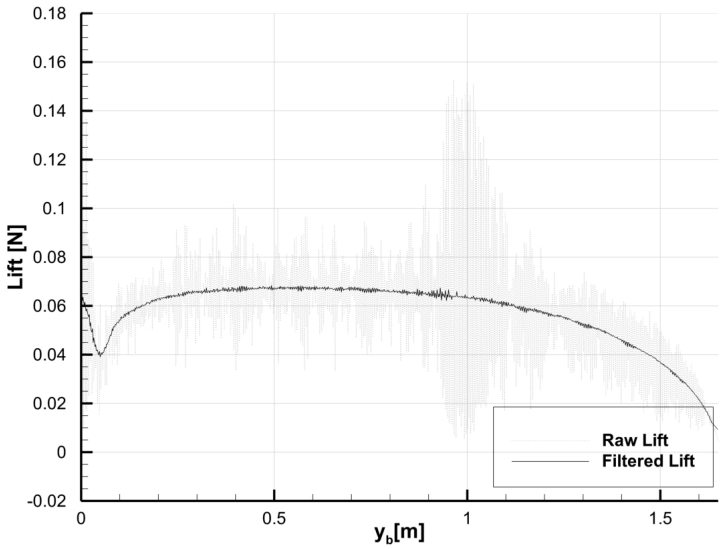

(a) Representation of lift distribution.

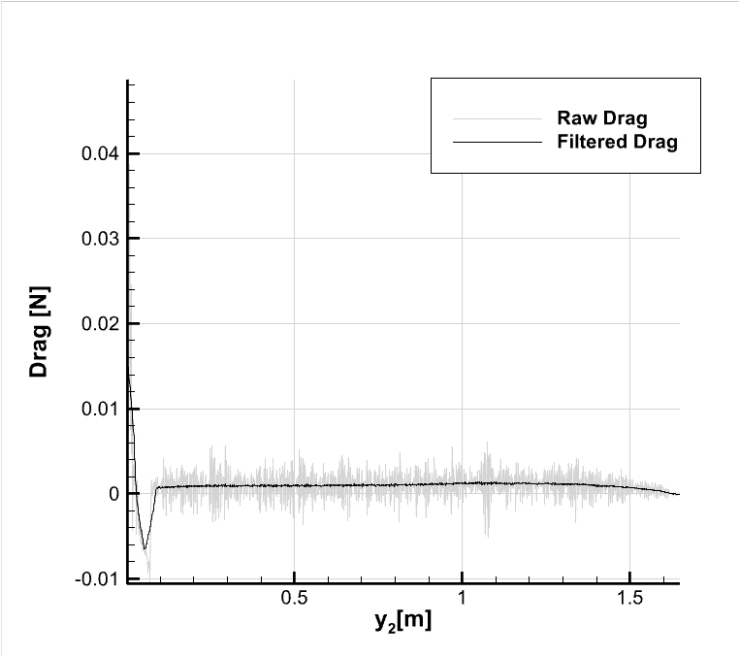

(b) Representation of drag distribution.

Figure C.4: Representation of lift and drag distributions for position number three.

Appendix D

Skin Friction Coefficient distribution for various configurations

In *Appendix D* the skin friction coefficients for all cases are graphically represented for consultation.

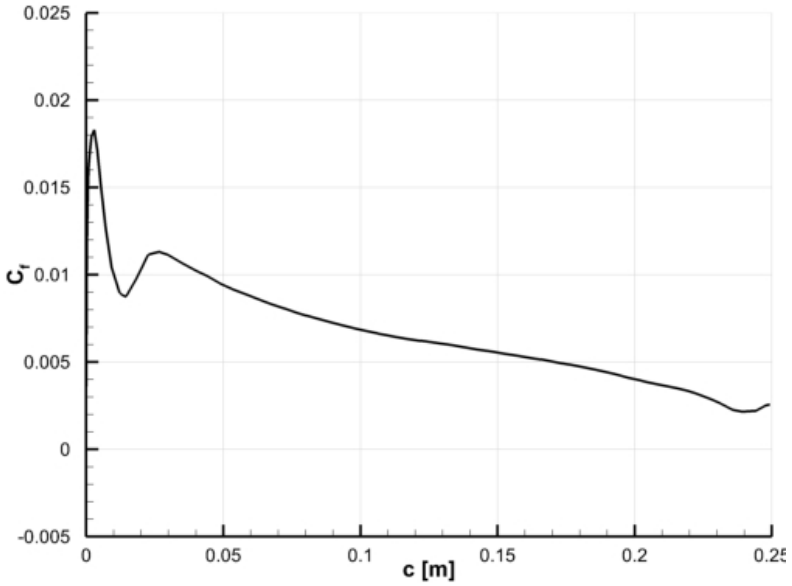

Figure D.1: Representation of skin friction coefficient for position two.

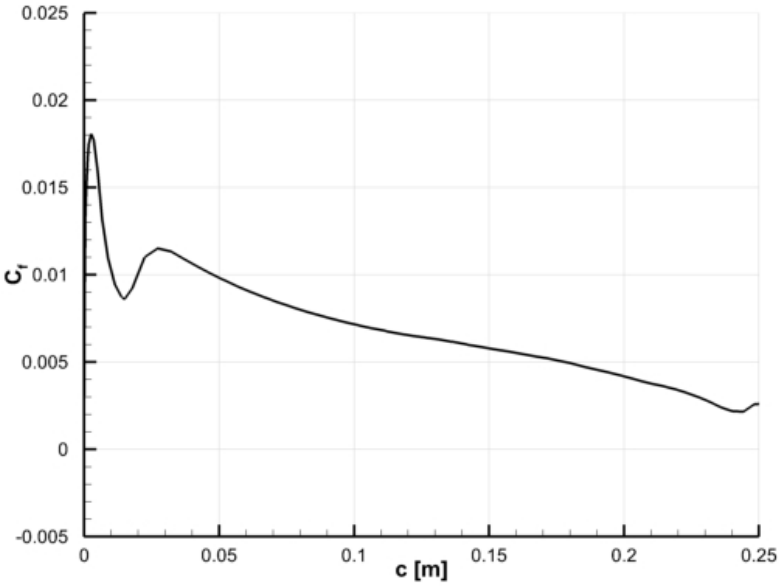

Figure D.2: Representation of skin friction coefficient for position five.

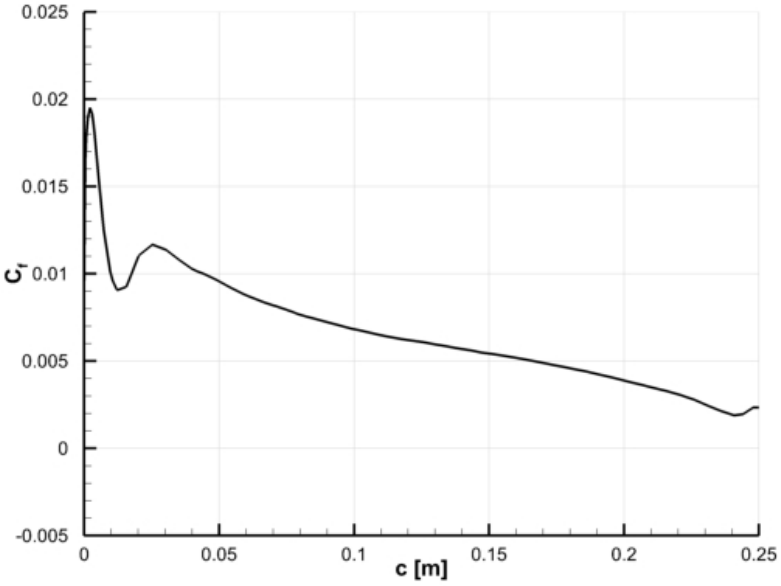

Figure D.3: Representation of skin friction coefficient for position one.

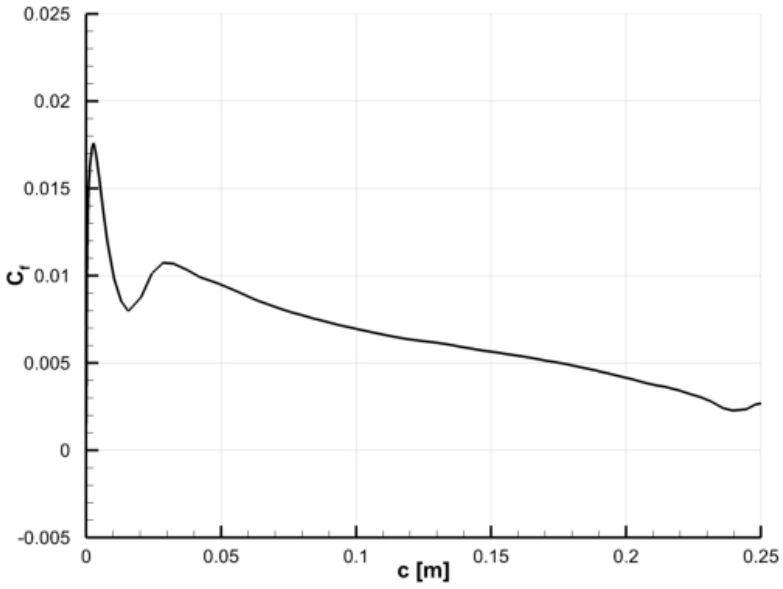

Figure D.4: Representation of skin friction coefficient for position three.